OncoLoop: A Network-Based Precision Cancer Medicine Framework

Alessandro Vasciaveo[1], Juan Martín Arriaga[2], Francisca Nunes de Almeida[2], Min Zou[2],
Eugene F. Douglass Jr[1], Florencia Picech[2], Maho Shibata[3,4,5], Antonio Rodriguez-Calero[6,7], Simone de Brot[8],
Antonina Mitrofanova[1], Chee Wai Chua[3,4,5], Charles Karan[1,9], Ronald Realubit[1,9], Sergey Pampou[1,9],
Jaime Y. Kim[2], Stephanie N. Afari[2], Timur Mukhammadov[2], Luca Zanella[1], Eva Corey[10], Mariano J. Alvarez[1,11],
Mark A. Rubin[6,12], Michael M. Shen[1,3,4,5,13], Andrea Califano[1,3,9,13,14,15], and Cory Abate-Shen[1,2,3,5,13,16]

ABSTRACT Prioritizing treatments for individual patients with cancer remains challenging, and performing coclinical studies using patient-derived models in real time is often unfeasible. To circumvent these challenges, we introduce OncoLoop, a precision medicine framework that predicts drug sensitivity in human tumors and their preexisting high-fidelity (cognate) model(s) by leveraging drug perturbation profiles. As a proof of concept, we applied OncoLoop to prostate cancer using genetically engineered mouse models (GEMM) that recapitulate a broad spectrum of disease states, including castration-resistant, metastatic, and neuroendocrine prostate cancer. Interrogation of human prostate cancer cohorts by Master Regulator (MR) conservation analysis revealed that most patients with advanced prostate cancer were represented by at least one cognate GEMM-derived tumor (GEMM-DT). Drugs predicted to invert MR activity in patients and their cognate GEMM-DTs were successfully validated in allograft, syngeneic, and patient-derived xenograft (PDX) models of tumors and metastasis. Furthermore, OncoLoop-predicted drugs enhanced the efficacy of clinically relevant drugs, namely, the PD-1 inhibitor nivolumab and the AR inhibitor enzalutamide.

SIGNIFICANCE: OncoLoop is a transcriptomic-based experimental and computational framework that can support rapid-turnaround coclinical studies to identify and validate drugs for individual patients, which can then be readily adapted to clinical practice. This framework should be applicable in many cancer contexts for which appropriate models and drug perturbation data are available.

INTRODUCTION

Systematic prediction of drug efficacy *in vivo* remains a major clinical challenge for most cancer types due, in part, to tumor heterogeneity, which makes it difficult to optimize treatments on an individual basis. This is further compounded by difficulties in establishing patient-derived models that recapitulate the biology and complexity of an individual patient's tumor for coclinical validation. Indeed, for some tumor types, the establishment of patient-derived xenograft (PDX) models can take more than 1 year (1, 2), thus compromising their usefulness for evaluating

drug efficacy within a timeframe compatible with patient care, especially in the metastatic setting. Patient-derived organoid (PDO) models have become increasingly more accessible and representative; however, these may not effectively model the tumor microenvironment (3, 4). Although human tumor cell lines are widely available for many cancer types, they rarely represent the full spectrum of tumor phenotypes observed in patients and often have idiosyncratic dependencies, as a result of alterations they accrue to survive *in vitro*. In principle, genetically engineered mouse models (GEMM), which are now widely available for many cancer types (5), may be valuable for studying

[1]Department of Systems Biology, Vagelos College of Physicians and Surgeons, Columbia University Irving Medical Center, New York, New York. [2]Department of Molecular Pharmacology and Therapeutics, Vagelos College of Physicians and Surgeons, Columbia University Irving Medical Center, New York, New York. [3]Department of Medicine, Vagelos College of Physicians and Surgeons, Columbia University Irving Medical Center, New York, New York. [4]Department of Genetics and Development, Vagelos College of Physicians and Surgeons, Columbia University Irving Medical Center, New York, New York. [5]Department of Urology, Vagelos College of Physicians and Surgeons, Columbia University Irving Medical Center, New York, New York. [6]Department for Biomedical Research, University of Bern, Bern, Switzerland. [7]Institute of Pathology, University of Bern and Inselspital, Bern, Switzerland. [8]COMPATH, Institute of Animal Pathology, University of Bern, Bern, Switzerland. [9]J.P. Sulzberger Columbia Genome Center, Columbia University Irving Medical Center, New York, New York. [10]Department of Urology, University of Washington, Seattle, Washington. [11]DarwinHealth Inc., New York, New York. [12]Bern Center for Precision Medicine (BCPM), Bern, Switzerland. [13]Herbert Irving Comprehensive Cancer Center, Columbia University Irving Medical Center, New York, New York. [14]Department of Biochemistry and Molecular Biophysics, Vagelos College of Physicians and Surgeons, Columbia University Irving Medical Center, New York, New York. [15]Department of Biomedical Informatics, Vagelos College of Physicians and Surgeons, Columbia University Irving Medical Center, New York, New York. [16]Department of Pathology and Cell Biology, Vagelos College of Physicians and Surgeons, Columbia University Irving Medical Center, New York, New York.

Corresponding Author: Andrea Califano, Department of Systems Biology, 1130 Saint Nicholas Avenue, Vagelos College of Physicians and Surgeons, Columbia University Irving Medical Center, New York, NY 10032. Phone: 212-851-5183; E-mail: ac2248@cumc.columbia.edu

drug response in the whole organism in the context of the native tumor microenvironment. However, their effective use in coclinical studies requires an accurate assessment of their fidelity to their human counterparts in terms of recapitulating the biology and drug sensitivity of patient tumors (6).

These challenges are exemplified in prostate cancer, which remains the most prevalent form of cancer and a leading cause of cancer-related death in men (7). Prostate cancer is characterized by its wide range of disease outcomes; indeed, whereas men with locally invasive disease—accounting for the vast majority of new diagnoses—have a 5-year survival rate of >90%, those who progress to advanced prostate cancer have a 5-year survival rate of <30%. The first-line treatment for advanced prostate cancer is androgen deprivation therapy, which initially leads to tumor regression but ultimately to the emergence of castration-resistant prostate cancer (CRPC), which is often metastatic (mCRPC; refs. 8–10). Stand-ard-of-care second-line treatments include taxane-based chemotherapy, such as cabazitaxel, and second-generation antiandrogens, such as enzalutamide; although these may be initially effective, many patients fail treatment, leading to the emergence of highly aggressive disease variants, including neuroendocrine prostate cancer (NEPC; refs. 11, 12). Challenges in treating advanced prostate cancer include its inherent heterogeneity, the infrequency of driver mutations, and its long mutational tail (13), which make it difficult to determine *a priori* whether specific treatments are likely to be effective for any given patient. Furthermore, although there is an abundance of mouse models of prostate cancer (14), it has proven difficult to model human prostate cancer because the establishment of PDX and PDO models has been low yield, especially for advanced disease (15–19).

To overcome these challenges, we developed OncoLoop, a framework that integrates experimental and computational data to first identify high-fidelity models for a given human tumor (cognate model, hereafter), then predict optimal drug treatments for the patient and its cognate model based on large-scale drug perturbation profiles, and lastly validate drug efficacy using the cognate model. The rationale for OncoLoop is based on previous studies where we have shown that Master Regulator (MR) proteins represent mechanistic determinants of a tumor's transcriptional state and that MR-activity inversion effectively abrogates tumor viability (20–22). Thus, cognate models for a given patient are identified by assessing the conservation of MR protein activity for a patient and potential cognate models (23, 24); conversely, optimal drugs are prioritized based on their ability to invert the MR-activity signature of both a patient tumor and its

cognate models (21). Hence, OncoLoop identifies the most statistically significant three-way relationships encompassing a tumor, its highest fidelity cognate model(s), and one or more drugs predicted to invert the MR-activity signature of both tumor and cognate models (hereafter, MR-inverter drugs).

As a proof of concept, we established OncoLoop in the context of prostate cancer, for which both large-scale human patient cohorts—comprising both primary tumors and metas-tases (25, 26)—and an extensive repertoire of GEMMs (ref. 14 and this report) are available. Indeed, MR-conservation analy-sis revealed that a majority of patients in these cohorts were represented by at least one cognate GEMM-derived tumor (GEMM-DT). To identify MR-inverter drugs, we leveraged PanACEA (27), a large collection of drug perturbation pro-files in cell lines matched to 23 tumor subtypes, including prostate cancer cell lines. Three out of four predicted drugs prioritized by our analyses induced highly significant growth inhibition of tumor allografts from cognate GEMM-DTs *in vivo*. We further show that the predicted drugs are active in the castration-resistant contexts and enhanced the efficacy of the second-generation antiandrogen enzalutamide. Notably, we assessed the contribution of MR-inverter drugs toward rescuing inflammatory pathway activity and immunosensi-tivity—especially in the challenging and translationally rele-vant metastatic setting—by further validating predicted drugs in a cognate syngeneic model of metastasis in combination with a PD1 inhibitor, nivolumab. Finally, to confirm rel-evance to a human context, we further validated the predicted drugs in a cognate prostate cancer PDX tumor model. Taken together our findings show that OncoLoop provides an effec-tive framework for the rapid identification and evaluation of patient-relevant drugs in preexisting cognate models, thus supporting its coclinical application. OncoLoop is a highly generalizable framework that can be extended to other can-cers and potentially other diseases.
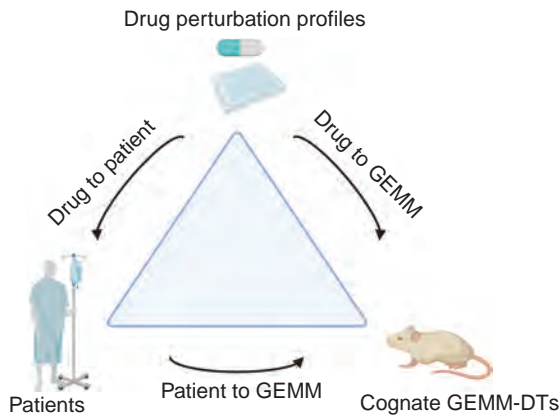
RESULTS
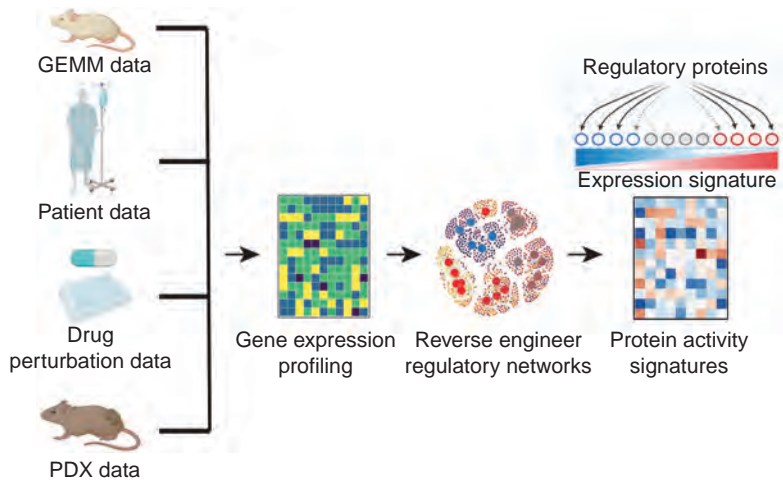
Conceptual Overview of OncoLoop

We developed OncoLoop for the purpose of identifying drugs poised to benefit patients, whose response could be evaluated in preexisting coclinical models (Fig. 1A). OncoLoop leverages regulatory networks reverse-engineered from large, tumor-specific RNA-seq profile datasets to first identify cog-nate models (i.e., GEMM-DTs) based on conservation of their MR-activity signature with a human tumor. In a second step, candidate MR-inverter drugs are prioritized by assessing their ability to invert the MR-activity signature of both the human tumor and its cognate GEMM-DTs based on drug

Figure 1. The OncoLoop conceptual framework. **A,** <u>Conceptual overview</u>: OncoLoop was designed to identify high-fidelity (cognate) models—in this study, GEMM-DTs—of a patient's tumor as well as drugs capable of inverting the MR protein activity for both the patient and their cognate GEMM-DT. To accomplish this, OncoLoop performs integrative analysis of transcriptomic (RNA sequencing) profiles from a patient's tumor, their cognate model, and drug perturbation assays. **B,** <u>Regulatory network analysis</u>: Gene expression profiles generated from each data source are used to reverse engineer species- and cohort-specific regulatory networks, which are then used to transform differential gene expression signature into differential protein activity profiles. **C,** <u>OncoLoop analysis</u>: Gene set enrichment analysis (GSEA) is used to assess the overlap in differentially active MR proteins between a human tumor and its cognate GEMM-DTs (OncoMatch). Similarly, GSEA is used to identify drugs capable of inverting the MR activity (MR-inverter drugs) for each patient and cognate GEMM-DT(s) pair. **D,** <u>Drug prediction and validation</u>: Representative Circos plot illustrating *PGD*-loops generated by matching a patient (*P*) to a GEMM-DT (*G*) and connecting them to each shared MR-inverter drug (*D*). Candidate drugs are first prioritized by pharmacotype analysis to identify the subset of patients predicted to be sensitive to the same subset of drugs and then validated *in vivo* using a cognate GEMM-DT–derived allograft, a syngeneic model of metastasis and a PDX model. (Created with BioRender.com.)
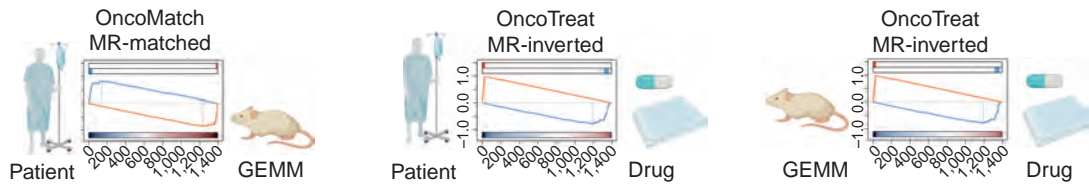
A OncoLoop conceptual framework

Drug perturbation profiles

Drug to patient

Drug to GEMM

Patient to GEMM

Patients

Cognate GEMM-DTs

B Regulatory network analysis

GEMM data

Patient data

Drug perturbation data

PDX data

Gene expression profiling

Reverse engineer regulatory networks

Regulatory proteins

Expression signature

Protein activity signatures

C OncoLoop analysis

OncoMatch MR-matched

Patient — GEMM

OncoTreat MR-inverted

Patient — Drug

OncoTreat MR-inverted

GEMM — Drug

D Drug prediction and validation

OncoLoop

P

D

G

Candidate drugs

1 2 3 4 5

In vivo validation

Allograft Syngeneic PDX
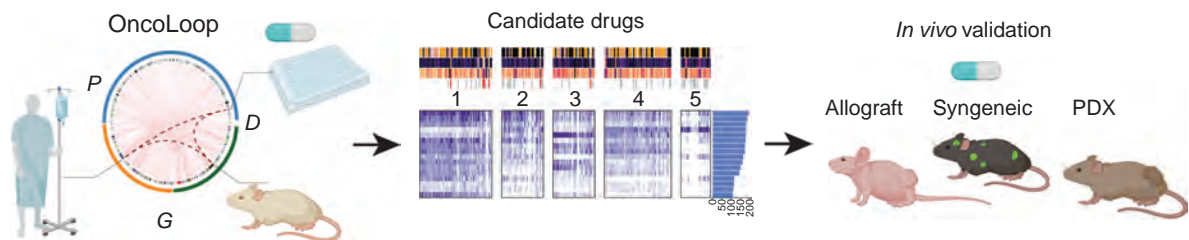
perturbation profiles of MR-matched tumor cell lines. Finally, the efficacy of predicted drugs is validated *in vivo* using the cognate models. We have established OncoLoop based on prostate cancer, for which we have generated a comprehensive series of GEMMs; however, for other cancer types, PDX models may be used if large, representative collections are available.

Data Generation

We leveraged large-scale RNA sequencing (RNA-seq) profiles from (i) our comprehensive series of GEMMs representing a broad spectrum of prostate cancer phenotypes (this study); (ii) publicly available RNA-seq profiles from primary tumors in The Cancer Genome Atlas (TCGA; ref. 25) and metastases in the Stand Up To Cancer–Prostate Cancer Foundation (SU2C; ref. 26) cohorts; (iii) large-scale drug perturbation profiles from MR-matched tumor cell lines (ref. 27 and this study); and (iv) RNA-seq profiles from well-characterized human prostate cancer PDX models (this study; Fig. 1B).

Protein Activity Analysis

OncoLoop requires accurate protein activity assessment for appraisal of MR-activity signatures, identification of cognate models, and prediction of MR-inverter drugs. This is accomplished using the VIPER algorithm (23), which transforms RNA-seq profiles into accurate protein activity profiles, as recently validated by antibody-based protein abundance measurements (28). Akin to a highly multiplexed gene reporter assay, VIPER uses the expression of a protein's tissue-specific targets (*regulon*) to measure its activity. The repertoire of targets of all regulatory and signaling proteins in a specific tissue context (i.e., context-specific interactome) is generated by reverse engineering large-scale, tissue-specific RNA-seq profiles using the ARACNe algorithm (29). Notably, to support accurate, model-specific protein activity measurements, we generated separate interactomes from patient-, GEMM-, and PDX-specific RNA-seq datasets (Fig. 1B).

GEMM Cohort Characterization and Cognate Model Identification

First, we analyzed VIPER-based protein activity profiles from the GEMM-DTs to identify molecularly distinct subtypes and to demonstrate their relevance to the disease spectrum of human prostate cancer. Next, we identified cognate GEMM-DTs, based on MR-activity signature conservation, for individual human primary prostate cancer tumors and metastases in the TCGA and SU2C cohorts, respectively (Fig. 1C). This revealed broad coverage, in which 78% and 93% of tumors and metastases were matched to at least one cognate GEMM-DT, respectively.

Assessing Drug Mechanism of Action in MR-Matched Cell Lines

To predict drug sensitivity, we leveraged human tumor–relevant drug perturbation profiles generated for two prostate cancer cell lines—the androgen-dependent LNCaP and the androgen-independent DU145 cell lines—that jointly provide high-fidelity models for >80% of the tumors in the TCGA cohort based on MR-activity signature conservation (ref. 27 and this study). To focus on patients with the more aggressive

mCRPC, we relied on RNA-seq profiles of DU145 cells that had been treated with a library of FDA-approved and late-stage experimental oncology drugs (i.e., drug perturbation profiles). Finally, the proteome-wide mechanism of action (MoA) of each drug was assessed using VIPER to measure the differential protein activity in drug-treated versus control-treated cells and used to identify optimal MR-inverter drugs for patient- and cognate GEMM-DT pairs (Fig. 1C). Note that contrary to conventional drug screening assays, OncoLoop does not rely on cell lines to assess drug sensitivity but only to elucidate drug MoA—that is, the effect of the drug on the activity of regulatory and signaling proteins.

Closing the Loop

Having "matched" each patient tumor (*P*) to a cognate GEMM-DT (*G*) and assessed each drug (*D*) as a potential MR-inverter for both a tumor and its cognate model, we ranked all (*P*, *G*, *D*) triplets (*PGD*-loops hereafter) based on the integration of three distinct *z*-scores, assessing the statistical significance of (i) the similarity of a patient and GEMM-DT MR-activity signature, (ii) the drug's MR-activity inversion as predicted from the patient tumor, and (iii) the drug's MR-activity inversion as predicted from the cognate GEMM-DT (Fig. 1C).

In Vivo Validation

To prioritize drug candidates of greatest translational relevance, we focused on clinically available drugs that were most frequently nominated by the analysis of the human tumor cohorts (i.e., pharmacotyping). Among these, we evaluated the ability of the top-predicted drugs to inhibit tumor growth and recapitulate the predicted MR-activity inversion *in vivo*, based on coclinical studies in cognate tumor allografts, a syngeneic model of metastasis, and a PDX tumor model (Fig. 1D). The following sections discuss each of these steps in detail.

A GEMM Resource That Models Prostate Cancer Progression

An essential requirement for OncoLoop is the availability of preexisting high-fidelity models—representing accurate surrogates for their human tumor counterpart—to enable coclinical validation of predicted drugs within a timeframe relevant to the patient's care. Toward this end, we assembled an extensive series of GEMMs that are based on genetic and/or pathway alterations that are prevalent in human prostate cancer and thereby recapitulate a broad spectrum of human prostate cancer phenotypes (Fig. 2A–E; Supplementary Fig. S1A–S1C; see Supplementary Detailed Materials and Methods; refs. 30–34). A complete list of GEMMs used in this study and a description of their individual tumor phenotypes is provided in Supplementary Table S1A and S1B; the entire GEMM series is available from The Jackson Laboratory (see Supplementary Table S1).

These GEMMs are based on the $Nkx3.1^{CreERT2}$ allele (Fig. 2A; ref. 35), which simultaneously introduces a prostate-specific inducible Cre driver and a heterozygous null allele for the $Nkx3.1$ homeobox gene, as is common in early-stage human prostate cancer (Supplementary Fig. S1A; ref. 25). We generated the baseline *NP* mice (for $\underline{Nkx3.1}^{CreERT2/+}$; $Pten^{flox/flox}$ mice) by crossing the $Nkx3.1^{CreERT2}$ allele with a
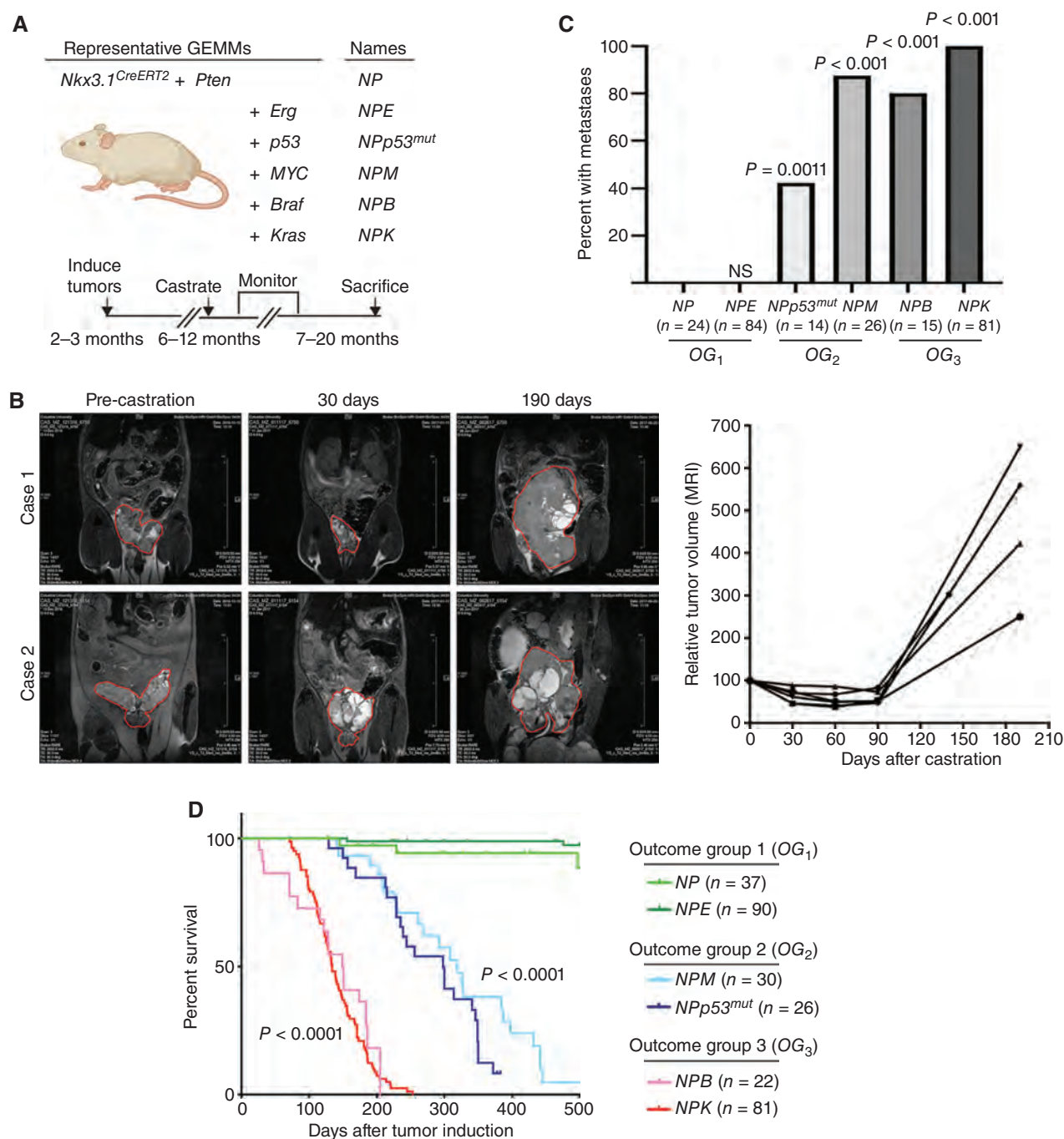
Figure 2. A GEMM resource that models prostate cancer progression. **A,** Schematic showing representative GEMMs used in this study. The GEMMs were generated by crossing *NP* mice (for $Nkx3.1^{CreERT2/+}$; $Pten^{flox/flox}$) with the alleles shown in the panel to generate six complex strains. The time line for tumor induction, castration, monitoring, and sacrificing is shown at the bottom of the panel. (Created with BioRender.com.) **B,** MRI images showing tumor volume changes after castration of 2 representative *NPp53* mice (case 1 and case 2). The plot on the right shows the tumor volume changes over time for 4 representative *NPp53* mice. **C,** Frequency of metastasis observed in the GEMMs. The numbers of mice used to determine metastasis frequency for each model are indicated in parentheses; two-tailed *P* values are shown for the Fisher exact test comparing each model to the *NP* mice (control). OG, outcome group. **D,** Kaplan–Meier survival analysis is shown for the models in the three outcome groups (OG_1, OG_2, and OG_3). *P* values were calculated using a two-tailed log-rank test compared with the *NP* mice (control). For the analyses shown in **C** and **D**, both intact and castrated mice were pooled for all GEMMs except *NPM*, where the effects of castration may be confounded by the AR dependency of the Probasin promoter used to drive Myc expression (see Supplementary Detailed Materials and Methods). (*continued on next page*)

Pten conditional allele (Fig. 2A; ref. 36) because *PTEN* mutations are prevalent from the earliest to most advanced stages of human prostate cancer (Supplementary Fig. S1A; refs. 25, 26). The *NP* mice were then crossed with various other alleles to model: (i) upregulation of *Erg* in the *NPE* mice (*E* for $Rosa26^{ERG/ERG}$; ref. 37); (ii) a missense mutation of *Tp53* in the
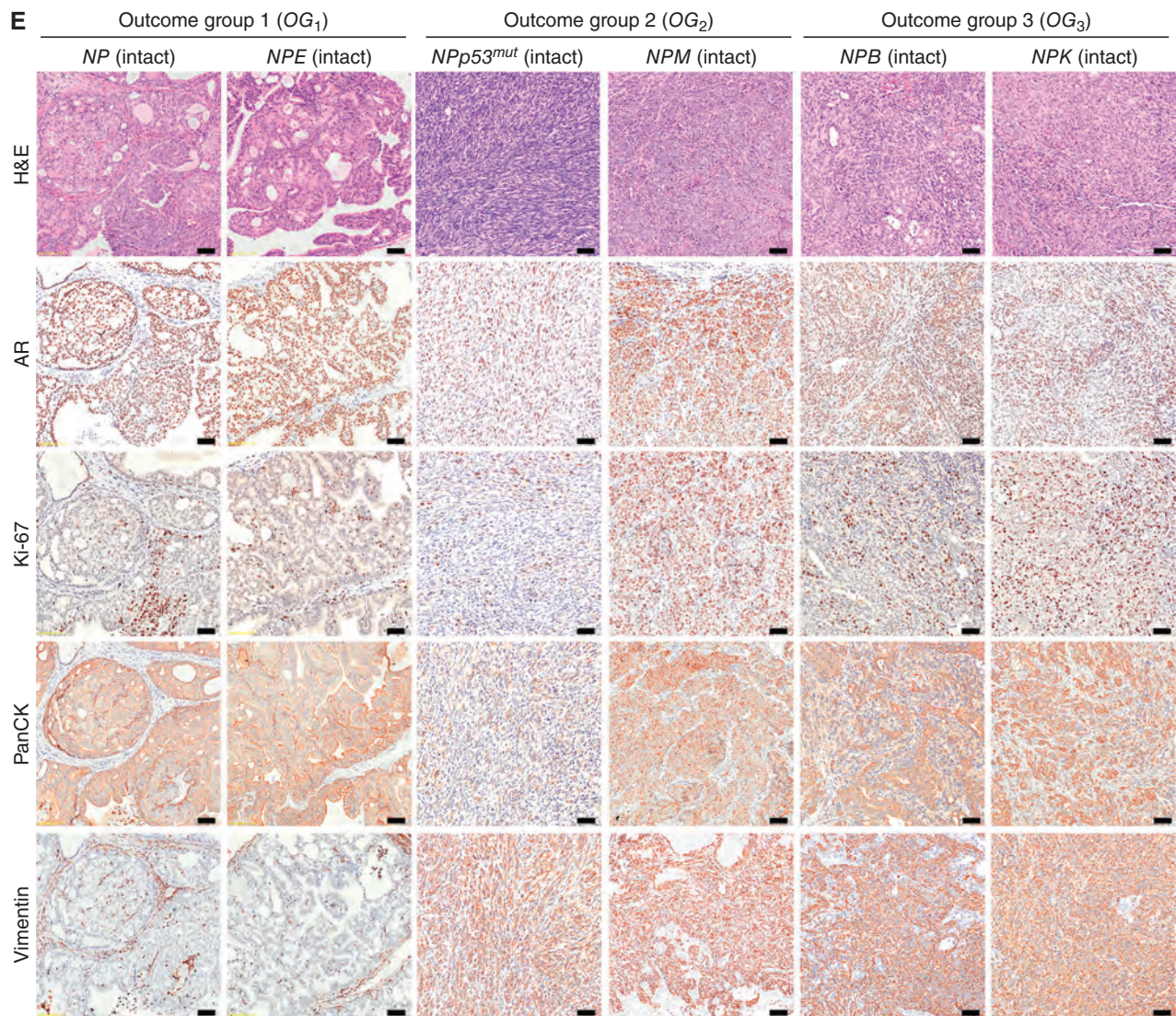
Figure 2. *(Continued)* **E,** Representative images for hematoxylin and eosin (H&E; top row) and IHC staining of the indicated markers in primary tumors from intact mice of the different GEMMs. Shown are representative images based on analyses of 3 or more mice/group; scale bars represent 50 µm. See also Supplementary Table S1 and Supplementary Figs. S1–S3. PanCK, pan-cytokeratin.

NPp53[mut] mice (for *Trp53*[LSL-R270H/flox]; ref. 38); (iii) upregulation of *c-Myc* in the *NPM* mice (*M* for *Hi-Myc;* ref. 39); (iv) an activating mutation of *Braf* in the *NPB* mice (B for *B-Raf*[V600E]; ref. 40; and (v) an activating mutation of *Kras* in the *NPK* mice (K for *Kras*[LSL-G12D]; ref. 41; Fig. 2A). These GEMMs also incorporate a conditionally activatable fluorescent reporter, the *Rosa26-CAG*[LSL-EYFP] allele (42), for high-efficiency lineage marking of tumors and metastases (30, 34).

Because tumor induction is based on an inducible Cre, expression of the relevant alleles following Cre-mediated gene recombination is not dependent on androgens, with the exception of the *Hi-Myc* allele, which is under the control of a constitutive *Probasin* promoter (39). Consequently, we could analyze tumor progression in both hormone-intact and castrated contexts (Fig. 2B–E; Supplementary Fig. S2A). As expected, the more indolent tumors regressed following castration, whereas the more aggressive ones developed progressive phenotypes

consistent with CRPC (Fig. 2B–E; Supplementary Fig. S2A; Supplementary Table S1A and S1B). In particular, as evident by MRI of *NPp53* mice, surgical castration leads to initial tumor regression followed by the eventual outgrowth of castration-resistant tumors (Fig. 2B). These phenotypic differences in intact and castrated tumors were evident by immunostaining for AR, which is expressed in and localized to nuclei in intact tumors but is diminished in expression in the castrated tumors (compare Fig. 2E; Supplementary Fig. S2A). Therefore, this GEMM series recapitulates both hormone-sensitive and CRPC.

This GEMM cohort could be subdivided into three outcome groups (OG_1–OG_3) based on their castration sensitivity, metastatic phenotype, and overall survival (Fig. 2C–E; Supplementary Fig. S2A and S2B; Supplementary Table S1A and S1B). Those in OG_1, which include the *NP* and *NPE* mice, developed indolent, nonlethal, and nonmetastatic tumors

with mostly benign, prostatic intraepitelial neoplasia–like histology and low levels of proliferation, as evident by Ki-67 staining. Those in OG_2, including the $NPp53^{mut}$ and NPM mice, were characterized by lethality within 1 year, were prone to develop metastasis, and displayed highly heterogeneous and proliferative histopathologic phenotypes. Finally, those in OG_3, including the NPB and NPK mice, were characterized by lethality by 6 months of age, which was accompanied by highly penetrant metastasis and high-grade, poorly differentiated histopathology.

To facilitate coclinical investigations, we established allograft, syngeneic, and organoid models from representative GEMMs (Supplementary Fig. S3A and S3B; Supplementary Table S1A; see Supplementary Detailed Materials and Methods). Because the GEMMs used herein are in a mixed strain background, allografts were generated by implanting freshly collected primary tumors into the flank of nude mouse hosts and passaged at least twice prior to analysis. Organoids were generated by FACS-based isolation of lineage-marked primary tumor cells, which were then cultured *in vitro* for up to five passages (Supplementary Fig. S3B). The histopathology of the resulting allograft and organoid models was similar to the parental tumors from which they were derived (Supplementary Fig. S3A and S3B). Interestingly, although we were able to generate organoids from GEMMs in each outcome group (OG_1–OG_3), we were only able to generate allograft models from the OG_2 and OG_3 tumors, but not from indolent OG_1 tumors. Thus, we have generated an extensive resource of prostate cancer GEMMs, as well as established culturable and transplantable models of these GEMMs. Because the current study relies on coclinical analyses *in vivo*, we used the allograft rather than organoid models; however, we envision that the organoid models will be beneficial for future *in vitro* investigations. Furthermore, to assess predicted drug activity in an immunocompetent context, we established a syngeneic model of prostate metastasis, which was derived from a bone metastasis from an NPK^{EYP} GEMM (30) and propagated in immunocompetent C57BL/6 mice.

GEMM Subtypes Recapitulate Human Prostate Cancer Phenotypes

To characterize the molecular features of the GEMM cohort, we generated RNA-seq profiles from benign prostate tissue and prostate tumors from 136 individual mice. First, we reverse engineered a GEMM-specific ARACNe interactome from these RNA-seq profiles (Supplementary Table S2A; ref. 29). The resulting interactome outperformed our previously published mouse interactome, which was assembled from Illumina gene expression microarrays of a less comprehensive GEMM cohort (20). For example, bioactivity analysis—which assesses the ability of an interactome to recapitulate differential protein activity across distinct phenotypes—showed that differentially active proteins had significantly higher average normalized enrichment scores ($\mu_{NES,New} = 3.79$ in the new interactome vs. $\mu_{NES,Old} = 1.96$ in the previous one; $P < 2.2 \times 10^{-16}$, by two-sided Kolmogorov–Smirnov test; Supplementary Fig. S4A; see Supplementary Detailed Materials and Methods). For instance, although the AR regulon—a critical determinant of prostate differentiation and tumorigenesis (43)—was a poor predictor of AR activity in the previous interactome (20), it was highly predictive in the new one (see Supplementary Figs. S3A, S4B–S4D, and S5A–S5C).

To define GEMM molecular subtypes and to assess their relationship to human prostate cancer, we focused on a subset of 91 GEMM-DTs having the most physiologically relevant histopathologic phenotypes (Supplementary Table S1B). We first transformed their RNA-seq profiles to VIPER-measured protein activity profiles using the GEMM prostate cancer interactome, and then performed protein activity–based cluster analysis (Fig. 3A; Supplementary Table S2B; see Supplementary Detailed Materials and Methods). To generate the differential gene expression signatures necessary for VIPER analysis, we compared each sample to the average of all 91 samples, thus identifying proteins with the greatest differential activity across all GEMM-DTs. Protein activity–based cluster analysis, which significantly outperforms gene expression–based clustering (22) identified five clusters, corresponding to five molecularly distinct subtypes (C_1–C_5) associated with disease aggressiveness with respect to outcome and metastasis (Fig. 3A; Supplementary Fig. S4B; Supplementary Table S2C; see Supplementary Detailed Materials and Methods). In particular, subtypes C_1 and C_2 mainly comprise tumors from the indolent outcome group (OG_1), whereas subtypes C_3 to C_5 comprise tumors from the two more aggressive outcome groups (OG_2 and OG_3). Consistent with these findings, the C_3 to C_5 subtypes were enriched for GEMMs with genomic alterations commonly associated with more aggressive human prostate cancer (Supplementary Table S2C).

Notably, >90% of the tumors in C_4 and C_5 had progressed to metastases compared with only 50% of those in C_3 and 11% of those in C_1 and C_2 (Fig. 3A; Supplementary Fig. S4B). Furthermore, the most indolent subtype, C_1, is mostly comprised of tumors that regressed following castration, whereas C_2 is mostly comprised of hormone-sensitive, indolent tumors; in contrast, C_3 to C_5 mostly comprise tumors from the more aggressive outcome groups, including both hormone-sensitive and castration-resistant ones (Fig. 3A; Supplementary Table S2C). Interestingly, AR activity was well correlated with gene expression in the more indolent clusters (C_1 and C_2) and progressively inactivated and less correlated with gene expression in more aggressive clusters (C_3 to C_5; Supplementary Fig. S5A), consistent with defects in nuclear localization, post-translational inactivation, and transcriptional competency in CRPC that decouple its expression and activity.

With respect to their molecular phenotypes, C_1 to C_5 tumors were characterized by aberrant activity of novel MR protein sets that effectively distinguished each subtype (Fig. 3A). These include homeodomain proteins (e.g., CDX1, PDX1, NKX2.6, NKX3.1, and PITX1) and other transcriptional regulatory proteins (e.g., GATA5, SOX15, and SOX7) that have known roles in cellular differentiation and cell lineage control in other tissue contexts. The coordinated switch between the molecular programs regulated by the top MR protein activities of each subtype was evident by the striking differential expression of the transcriptional targets of the most differentially active MRs of each subtype (Fig. 3B; Supplementary Fig. S6). As expected, CRPC tumors, such as those from the NPK and $NPp53^{mut}$ GEMMs, have a distinct MR-activity profile when compared with the corresponding intact tumors (Supplementary Fig. S5B).

Although the topmost significantly active MRs in subtypes C_1 to C_5 are novel, the differential activity of MR proteins with
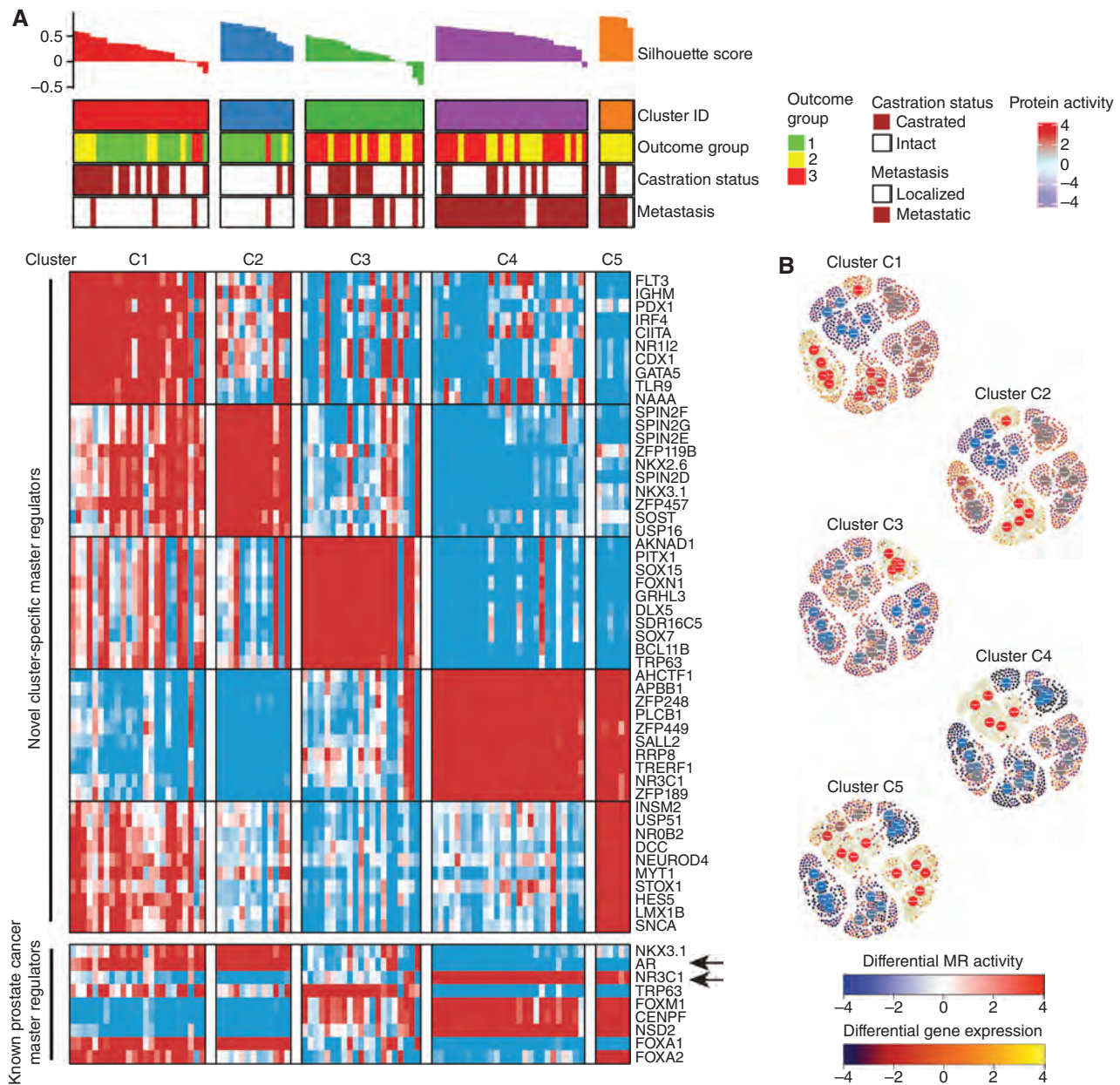
Figure 3. GEMM subtypes recapitulate human prostate cancer phenotypes. **A,** Heat map illustrating the results of protein activity–based cluster analysis of 91 GEMM-DTs, as well as the silhouette score and correlative variables, such as outcome group, castration status, and metastatic progression. Shown are five molecularly distinct clusters (C_1–C_5) that cosegregate with survival and metastatic potential. Indicated for each cluster are the 10 most significantly activated MRs (top heat map), and the activity levels of nine established human prostate cancer markers (bottom heat map). Arrows indicate the activities of Ar and glucocorticoid receptor (Nr3c1), which are inversely correlated. **B,** Representative subnetworks, representing the activity of the 25 most differentially active MR proteins (five per cluster, large circles) across all clusters and the expression of their regulatory targets (small circles) on a cluster-by-cluster basis. Protein activity is shown using a blue (inactivated) to red (activated) scale, whereas target expression is shown on a blue (underexpressed) to yellow (overexpressed) scale. High-resolution images with full visibility of the MRs are shown in Supplementary Fig. S5. See also Supplementary Table S2 and Supplementary Figs. S4–S6.

an established role in human and mouse prostate cancer progression was clearly evident (Fig. 3A; Supplementary Fig. S4C). In particular, the indolent subtypes C_1 and C_2 present high activity of NKX3.1, p63, and AR, which are associated with well-differentiated prostate cancer (43). In contrast, the most aggressive and highly metastatic subtypes, C_4 and C_5, present high activity of FOXM1, CENPF, and NSD2, which are all aberrantly activated and functionally necessary for aggressive

prostate cancer, in both humans and mice (20, 44). Notably, the aggressive subtypes C_4 and C_5 display downregulation of AR and coordinated upregulation of the glucocorticoid receptor (NR3C1), which is known to be activated in human CRPC (ref. 45; Fig. 3A; Supplementary Fig. S4C and S4D; Supplementary Fig. S5C). Interestingly, subtype C_5 presented dysregulation of proteins associated with NEPC, including aberrant FOXA2 activation and FOXA1 inactivation (Fig. 3A; Supplementary

Fig. S4C; ref. 46), and was significantly enriched in the Beltran NEPC signature ($P < 10^{-4}$; see Supplementary Detailed Materials and Methods; ref. 11), whereas no enrichment for the NEPC signature was detectable in subtypes C_1 to C_4. Notably, none of the GEMM-DTs, including those associated with advanced prostate cancer and NEPC (C_4 and C_5, respectively), had undergone pharmacologic treatment; this is a novel feature of the GEMM cohort compared with analogous human prostate cancer cohorts, which are generally derived from patients who had undergone extensive treatments (26).

To further characterize the GEMM subtypes and to assess their relationship to human prostate cancer, we performed pathway enrichment analyses (Supplementary Table S2D; see Supplementary Detailed Materials and Methods). To determine the top pathways associated with each subtype, we computed the enrichment of each gene set in proteins differentially active in each sample and then integrated across samples in each cluster using the Stouffer method (see Supplementary Detailed Materials and Methods). These analyses revealed that the most aggressive subtypes, C_4 and C_5, show strong enrichment for proliferation and oncogenic hallmarks, for example, G_2–M checkpoint ($P = 2.14 \times 10^{-39}$), E2F targets ($P = 4.5 \times 10^{-88}$), DNA repair ($P = 5.8 \times 10^{-68}$), and MYC targets V1 and V2 (integrated $P = 3.3 \times 10^{-21}$; Supplementary Fig. S4D; Supplementary Table S2D). (Note that all P values reported in this article are corrected for multiple hypothesis testing; see Supplementary Detailed Materials and Methods). Furthermore, as expected based on human prostate cancer, hormone-related pathways, including AR and glucocorticoid receptor–related pathways, were coordinately regulated and inversely correlated (Supplementary Fig. S4D; Supplementary Table S2D). Interestingly, interferon and inflammatory response hallmarks, including IFNα response ($P = 2.4 \times 10^{-52}$), IFNγ response ($P = 8.2 \times 10^{-68}$), and inflammatory response ($P = 4.7 \times 10^{-18}$) were downregulated in subtypes C_4 and C_5 (Supplementary Fig. S4D; Supplementary Table S2D). These findings suggest that the most aggressive tumors may have an immunosuppressive tumor microenvironment and therefore may be valuable for evaluating immunotherapy response.

Taken together, these molecular analyses define a series of GEMM subtypes (C_1 – C_5) that (i) are distinguished by novel as well as known MR protein activities; (ii) model a wide range of prostate cancer phenotypes from indolent to aggressive variants; (iii) model hormone responsivity as occurs in human prostate cancer, including castration-sensitive and castration-resistant tumors; (iv) can differentiate lethal subtypes of adenocarcinoma and NEPC in the absence of prior treatment; and (v) recapitulate key aspects of human prostate cancer, including expression of relevant MR proteins and relevant pathways. Thus, this GEMM cohort represents a valuable resource to characterize and model human prostate cancer, particularly for advanced tumors, as would be the principal focus for predicting drug treatments for human patients.

Matching GEMM-DTs to Patient Tumors and Metastases

Having established that the molecular programs of the GEMM cohort are relevant for human prostate cancer, we next asked whether individual GEMM-DTs can provide high-fidelity (cognate) surrogates for individual patients (Fig. 4A and B; see Supplementary Detailed Materials and Methods). We thus compared the MR protein activity signature for individual human patients with that of each available GEMM-DT ($n = 91$) and designated those presenting highly significant conservation of patient-specific MR activity ($P \leq 10^{-5}$, by one-tailed aREA test) as cognate models. For these studies, we queried two well-characterized patient cohorts, one comprised of treatment-naïve primary tumors collected by TCGA ($n = 333$; ref. 25) and a second comprised of posttreatment metastatic biopsies from mCRPC patients collected as part of the Stand Up To Cancer–Prostate Cancer Foundation cohort (SU2C; $n = 212$; ref. 26).

First, we assembled distinct human prostate cancer interactomes for the primary tumors and metastases by ARACNe analysis of RNA-seq profiles from the TCGA and SU2C cohorts, respectively (Supplementary Table S3A and S3B; see Supplementary Detailed Materials and Methods). We then used VIPER to transform the transcriptional profiles of the TCGA and SU2C cohorts into protein activity profiles, using their respective interactomes (Supplementary Table S3C and S3D). Differential expression signatures for VIPER analysis were computed using as reference a combination of all RNA-seq profiles from the Genotype-Tissue Expression (GTEx) normal prostate cohort ($n = 245$; ref. 47) and a humanized version of normal mouse prostate tissue (see Supplementary Detailed Materials and Methods). This approach allowed the identification of MR proteins that are specifically dysregulated in the tumor context compared with normal prostate.

To identify cognate models on an individual patient basis, we generated protein activity signatures by comparing each GEMM-DT to the same reference as above. We then assessed the fidelity of each of the GEMM-DTs to each individual TCGA or SU2C patient by assessing the enrichment of the 25 most activated ($25\uparrow$) and 25 most inactivated proteins ($25\downarrow$) of each human tumor, representing its candidate MR proteins (MR proteins hereafter for simplicity), compared with MR proteins differentially active/inactive in each GEMM-DT (Fig. 4A and B; Supplementary Table S4A and S4B). We used a fixed number of MR proteins (i.e., $25\uparrow+25\downarrow$) because (i) this is required to make the statistics of enrichment analyses comparable across proteins and cohorts, and (ii) we have previously shown that an average of 50 MRs is sufficient to account for the canalization of functionally relevant genetic alterations in the vast majority of TCGA samples (22). For simplicity, we refer to these $25\uparrow+25\downarrow$ MR proteins as the MR-activity signature. Having assessed the enrichment of their MR-activity signatures, we selected a highly conservative statistical threshold ($P \leq 10^{-5}$) to nominate high-fidelity, cognate GEMMs-DTs (see Supplementary Detailed Materials and Methods).

Analysis of primary tumors from the TCGA cohort revealed that 78% had at least one high-fidelity cognate GEMM-DT ($n = 261/334$; Fig. 4A; Supplementary Table S4A). Strikingly, analysis of prostate cancer metastases from the SU2C cohort revealed an even greater fraction (93%) of patients with high-fidelity cognate GEMM-DTs ($n = 198/212$), and, on average, 48 cognate GEMM-DTs were identified as significant cognate models ($P \leq 10^{-5}$) for each SU2C tumor (Fig. 4A; Supplementary Table S4B). This likely reflects the inherent bias of the GEMM cohort toward more aggressive
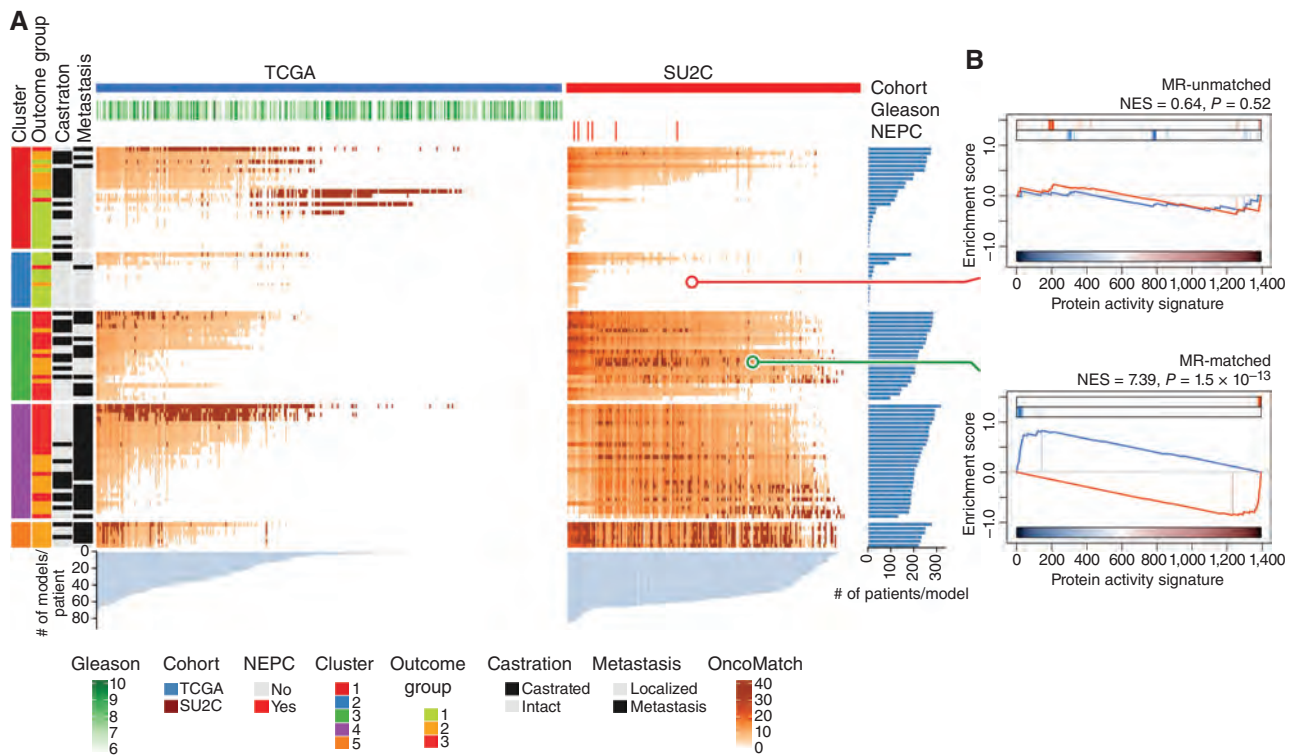
Figure 4. Matching GEMM-DTs to patient tumors and metastases. **A,** Heat maps represent the MR-based fidelity score of each tumor sample (columns) vs. each GEMM-DT model (rows) for the TCGA (right) and SU2C (left) cohort, respectively. Relevant patient phenotypic variables—that is, cohort, Gleason score, and NEPC status—are shown in the top three bars, whereas relevant GEMM-DT phenotypic variables—that is, cluster, outcome, castration status, and metastasis status—are shown in the four vertical bars to the left of the heat map. Fidelity scores are computed as the $-\mathrm{Log}_{10}P$ of the patient vs. GEMM-DT MR enrichment analysis. The five topmost significant cognate models for each patient are shown in dark red; other statistically significant ($P \le 10^{-5}$) high-fidelity models are shown using a lighter to darker color scale (as shown). The light blue bar plots at the bottom of the two heat maps show the number of candidate cognate models for each patient, whereas the dark blue bar plots to the right show the number of patients for which a GEMM-DT represents a cognate model. Overall, 78% of the samples in the TCGA ($n = 261$ of 334) and 93% of those in the SU2C cohorts ($n = 198$ of 212) have at least one cognate GEMM-DT. **B,** Gene set enrichment analysis of the fidelity analysis for representative GEMM-DT–SU2C pairs showing an example of an MR-unmatched (low-fidelity, top) and an MR-matched (high-fidelity, bottom) pair. See also Supplementary Table S4. NES, normalized enrichment score.

prostate cancer phenotypes (see Fig. 3). Heat map representation of the matched patients and GEMM-DTs shows good clustering of patient and GEMM-DTs in the same subtype (C_1–C_5). Although most patients were matched to multiple GEMM-DTs, we highlight the GEMM-DTs representing the top five most statistically significant MR-based matches for each patient (i.e., the highest fidelity models, Fig. 4A) because these would provide the best models for coclinical studies. As expected, given the more aggressive nature of the SU2C patients, highest fidelity models for the TCGA and SU2C cohorts formed distinct clusters. These findings demonstrate that individual tumors from the GEMM cohort (GEMM-DTs) represent high-fidelity surrogates for individual patients with prostate cancer. Furthermore, most of the patients with aggressive prostate cancer, who would benefit most from coclinical validation of novel treatments *in vivo*, are represented by at least one GEMM-DT.

Generation of Drug Perturbational Profiles to Identify MR-Inverter Drugs

To generate drug perturbations for predicting optimal drug treatments, we first identified cell lines that most closely recapitulate the MR signature of the patients. Specifically, we performed VIPER analyses on gene expression signatures for each of the 10 prostate cancer cell lines available in the Cancer Cell Line Encyclopedia (CCLE), and compared these data with the corresponding data from the TCGA (Supplementary Fig. S7A–S7C) and SU2C (Supplementary Fig. S7D–S7F) cohorts (27). This analysis identified two prostate cancer cell lines—the androgen-dependent LNCaP and the androgen-independent DU145 lines—that jointly provided high-fidelity models for >80% of the tumors in the TCGA cohort based on MR-activity signature conservation (Supplementary Fig. S7A and S7D; ref. 27). Although drug predictions using either LNCaP or DU145 perturbation profiles were concordant (27), to identify optimal treatments for prostate cancer patients with aggressive tumors, our subsequent analyses focused primarily on the more aggressive, AR-independent DU145 cell line.

Specifically, drug MoA was assessed from RNA-seq profiles of DU145 or LNCaP cells harvested 24 hours following treatment with 117 FDA-approved and 218 late-stage experimental (i.e., in phase II and III clinical trial) drugs, as well as vehicle control (DMSO; i.e., $n = 335$ drugs in total, Supplementary Table S5A). To minimize activation of cell death or cellular stress pathways that would confound the assessment

of drug MoA, cells were treated with the 48-hour EC_{20} concentration of each drug (i.e., highest sublethal concentration), as assessed from 10-point drug response curves (see Methods). RNA-seq profiles were generated using PLATE-seq, which was specifically designed to generate profiles of drug perturbations by microfluidic automation (48).

For each drug, differential protein activity profiles, representing the drug's MoA, were then generated by VIPER analysis of drug versus vehicle control–treated cells (Supplementary Table S5B; see Supplementary Detailed Materials and Methods). Cluster analysis of differentially activated proteins following drug treatment with the most bioactive agents—that is, 115 drugs inducing the most significant differential protein activity patterns—identified 11 drug clusters (D_1–D_{12}) based on differential activation/inactivation of 13 protein sets (programs; P_1–P_{13}; Supplementary Fig. S8). Consistent with the analysis, drugs presenting similar MoA were clustered together or in closely related clusters. For instance, cytotoxic drugs cosegregated in clusters D_1, D_2, D_5, D_7, and D_8, whereas kinase inhibitors were found mostly in clusters D_3, D_{10}, and D_{12}, including a majority of MAPK (i.e., sorafenib, dabrafenib, vemurafenib, and trametinib), EGFR inhibitors (i.e., lapatinib, erlotinib, and vandetanib), and mTOR inhibitors (i.e., everolimus and temsirolimus) in D_{12}. Similarly, a subset of hormone blockade drugs (i.e., anastrazole, enzalutamide, abiraterone, and mitotane) clustered in D_6 and D_9 and another subset (i.e., raloxifene, leuprolide, exemestane, and tamoxifen) in D_3 and D_4. Folate (i.e., methotrexate and pralatrexate) and microtubule inhibitors (i.e., paclitaxel and ixabepilone) clustered in D_4, whereas proteasome inhibitors (i.e., ixazomib, carfilzomib, and bortezomib) presented very similar profiles in D_{11} and D_{12}. In contrast, as expected, more pleiotropic drugs with broad-spectrum MoA, such as HDAC inhibitors (i.e., vorinostat, panobinostat, and belinostat), CRBN inhibitors (i.e., thalidomide, lenalidomide, and pomalidomide), and demethylating agents (i.e., decitabine and azacytidine), were broadly distributed across multiple clusters. Given the high reproducibility of replicate perturbational profiles from the same drug ($P \ll 0.05$, by two-tail enrichment analysis), for the majority of the 115 bioactive compounds, and the diversity of the differential protein activity they induce, this suggests that the perturbational profiles generated for this study effectively inform on drug MoA (27).

Using OncoLoop to Predict Candidate Drugs for Individual Patients

To predict candidate drugs, we identified those for which the MR-activity signature of both a patient and its cognate GEMM-DT was significantly inverted in drug-treated versus vehicle control–treated cells (MR-inverter drugs; Fig. 5A–C). Because our goal is to identify treatments for patients with advanced, rather than indolent, prostate cancer, we focused on the metastatic patients in the SU2C cohort and their cognate GEMM-DTs (which could be identified for 93% of the SUC2 patients; see Fig. 4). For each SU2C patient and each cognate GEMM-DT, MR-inverter drugs were identified by enrichment analysis of the respective top 25↑ and 25↓ MR proteins (see Fig. 4) compared with the MR-activity signatures of the drug-treated versus vehicle control–treated

cells, at a conservative statistical threshold ($P \leq 10^{-5}$; Supplementary Table S5C and S5D).

The resulting PGD-loops—comprising a patient, its cognate GEMM-DT, and the candidate MR-inverter drugs (Fig. 5A and B)—were ranked based on the Stouffer integration of three z-scores, corresponding to (i) z_{PG}, the GEMM versus patient MR-activity conservation z-score (Supplementary Table S4B); (ii) z_{PD}, the patient-specific MR-inverter drug z-score (Supplementary Table S5C); and (iii) z_{GD}, the cognate GEMM-DT–specific MR-inverter drug z-score (Supplementary Table S5D). Considering all possible combinations of SU2C patients ($n = 212$), GEMM-DTs ($n = 91$), and drugs ($n = 337$), there were >6.5 million potential PGD-loops; of these, 668,138 achieved statistical significance ($P \leq 10^{-5}$) on all three z-scores (Supplementary Table S6). Notably, the extensive coverage of both GEMM-DTs and drugs for the SU2C patients, which on average was 48 cognate GEMM-DTs ($P \leq 10^{-5}$) for each SU2C tumor (see Fig. 4) and 22 FDA-approved candidate MR-inverters ($P \leq 10^{-5}$) for each SU2C tumor/cognate–GEMM-DT pair, supports the use of OncoLoop in a coclinical setting.

To provide a visual representation of OncoLoop, we show three heat maps reporting the statistical significance of model fidelity (OncoMatch), and drug MR-inversion analyses (OncoTreat) for a subset of SU2C patients ($n = 56$), their cognate GEMM-DTs ($n = 5$), and drugs ($n = 28$), which were especially enriched in statistically significant PGD-loops (Fig. 5A). For illustrative purposes, we highlight a PGD-loop defined by an mCRPC patient (SC_9182_T), his cognate GEMM-DT (CMZ315)—harboring mutation of $p53$, a gene that is frequently dysregulated in human CRPC (see Supplementary Fig. S1A)—and the MEK inhibitor trametinib (Fig. 5A and B). Notably, as evident by gene set enrichment analysis (GSEA), all three normalized enrichment score (NES) values for this PGD-loop were highly significant, including for the model fidelity analysis (NES = 8.14, $P = 4.1 \times 10^{-16}$), as well as for the patient-specific (NES = −5.47, $P = 4.4 \times 10^{-8}$) and cognate GEMM-DT–specific trametinib-mediated MR inversion (NES = −4.99, $P = 6.2 \times 10^{-7}$; Fig. 5C), resulting in a highly significant integrated, OncoLoop P value (NES = 10.71, $P = 4.6 \times 10^{-27}$).

Coclinical Validation in Cognate GEMM-DTs

To optimize the clinical translation of this approach and to capture OncoLoop predictions for a majority of patients, we focused on PGD-loops comprising drugs that were both clinically available and most recurrently predicted for SU2C patients (Fig. 5D). Specifically, we considered only FDA-approved drugs ($n = 117$), predicted for ≥50% of the SU2C tumors, and active at physiologically relevant concentrations (≤1 µmol/L), thus yielding 16 candidate drugs for validation. Cluster analysis of their MR-inversion z-score for individual SU2C tumors (i.e., predicted drug sensitivity) identified five clusters, representing subsets of patients predicted to be sensitive to the same subsets of drugs (i.e., pharmacotypes; see Methods; Fig. 5D). Independent stratification of the GEMM-DTs, also considering only FDA-approved drugs active at physiologically relevant concentrations (≤1 µmol/L), identified the same top 16 drugs (Fig. 5E), thus further confirming the representative nature of these cognate models. Consistent
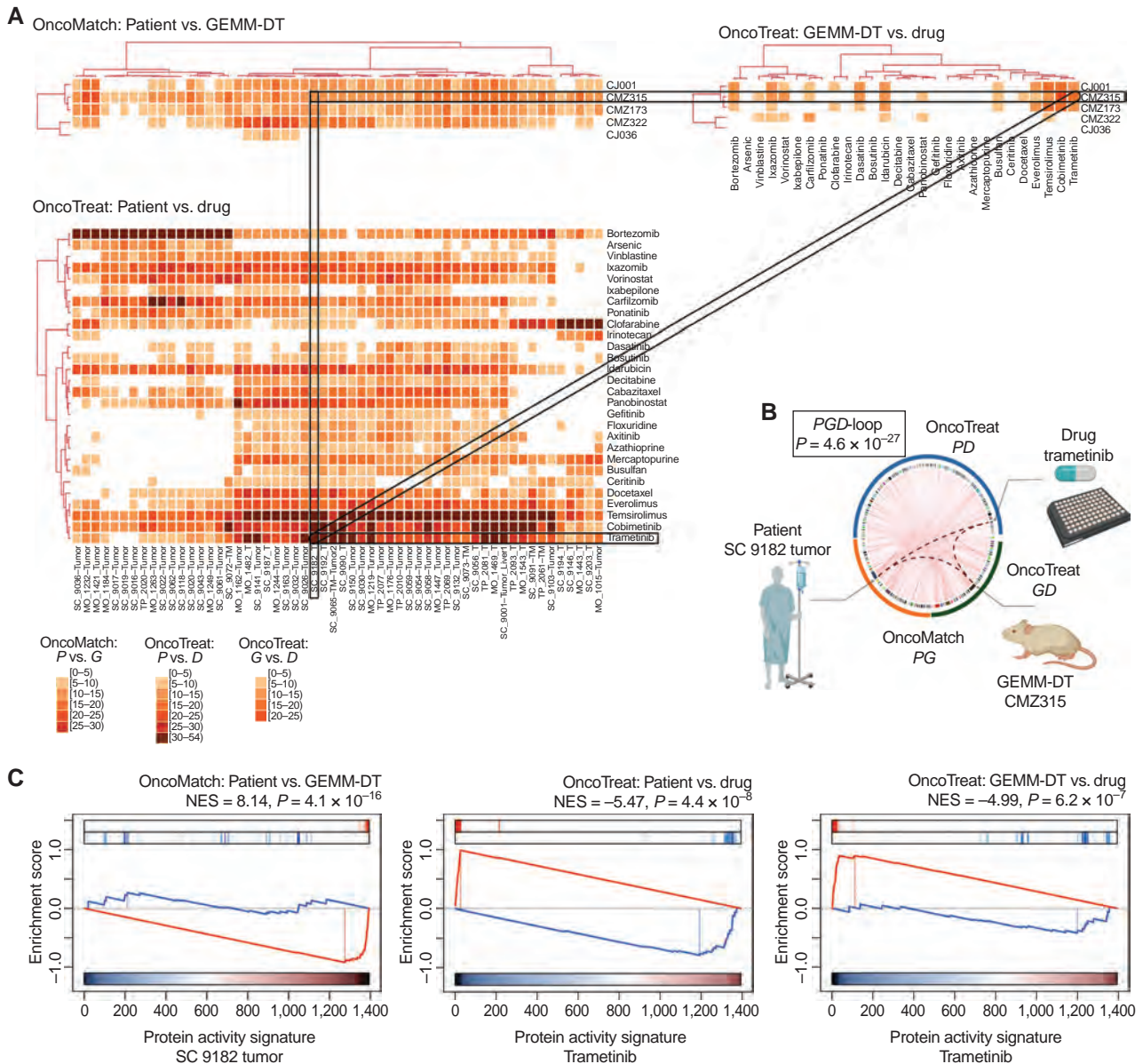
Figure 5. OncoLoop analysis. **A,** Illustrative examples of a PGD-loop: three heat maps representing a subset of patients, GEMM-DTs, and drugs are shown. The top left heat map (OncoMatch: patient vs. GEMM-DT) shows the fidelity scores for 56 SU2C samples (columns) and five GEMM-DTs (rows); the bottom left heat map (OncoTreat: patient vs. drug) shows the MR-inverter scores for 28 drugs (rows), as assessed against 56 SU2C samples (columns); and finally, the top right heat map (OncoTreat: GEMM-DT vs. drug) shows the MR-inverter scores for the same 28 drugs (columns), as assessed against the five GEMM-DTs (rows). All scores are computed as ($-Log_{10}P$), and statistically significant scores ($P \leq 10^{-5}$) are shown with a light to dark color scale as indicated; nonsignificant scores are shown in white. MR-inverter scores are based on MR-activity inversion analysis based on the drug- vs. vehicle control–treated DU145 cells. For visualization purposes, heat map results are depicted by hierarchical clustering. Among the many statistically significant PGD-loops, we highlight one formed by the SU2C sample SC_9182_T, his top-ranked cognate GEMM-DT (CMZ315), and the drug trametinib. (Created with BioRender.com.) **B,** Circos plot showing all significant PGD-loops, including the one highlighted in **A** (thicker, dotted curves). P value calculated by integrating the three associated scores. **C,** GSEA plots for the three relationships in the highlighted PGD-loop, including (i) the patient to cognate GEMM-DT fidelity analysis (OncoMatch: patient vs. GEMM-DT, left), (ii) the MR-inversion score by trametinib, as assessed for the SU2C sample MRs (OncoTreat: patient vs. drug, middle), and (iii) the MR-inversion score by trametinib, as assessed for the cognate GEMM-DT (OncoTreat: GEMM-DT vs. drug, right). (continued on following page)

with our model fidelity-based expectations, pharmacotyping analyses using LNCaP perturbation profiles produced results that were similar to those from DU145 cells (Supplementary Fig. S9A and S9B).

Among the 16 prioritized drugs, we eliminated those with overlapping MoA (e.g., multiple HDAC inhibitors) or lacking

demonstrated variable efficacy in prior prostate cancer clinical trials, thus yielding four candidate drugs for experimental validation: temsirolimus (mTOR inhibitor; NCT00919035 and NCT00012142; ref. 49), trametinib (MEK inhibitor; NCT02881242 and NCT01990196), panobinostat (HDAC inhibitor; NCT00667862 and NCT00878436; ref. 50), and
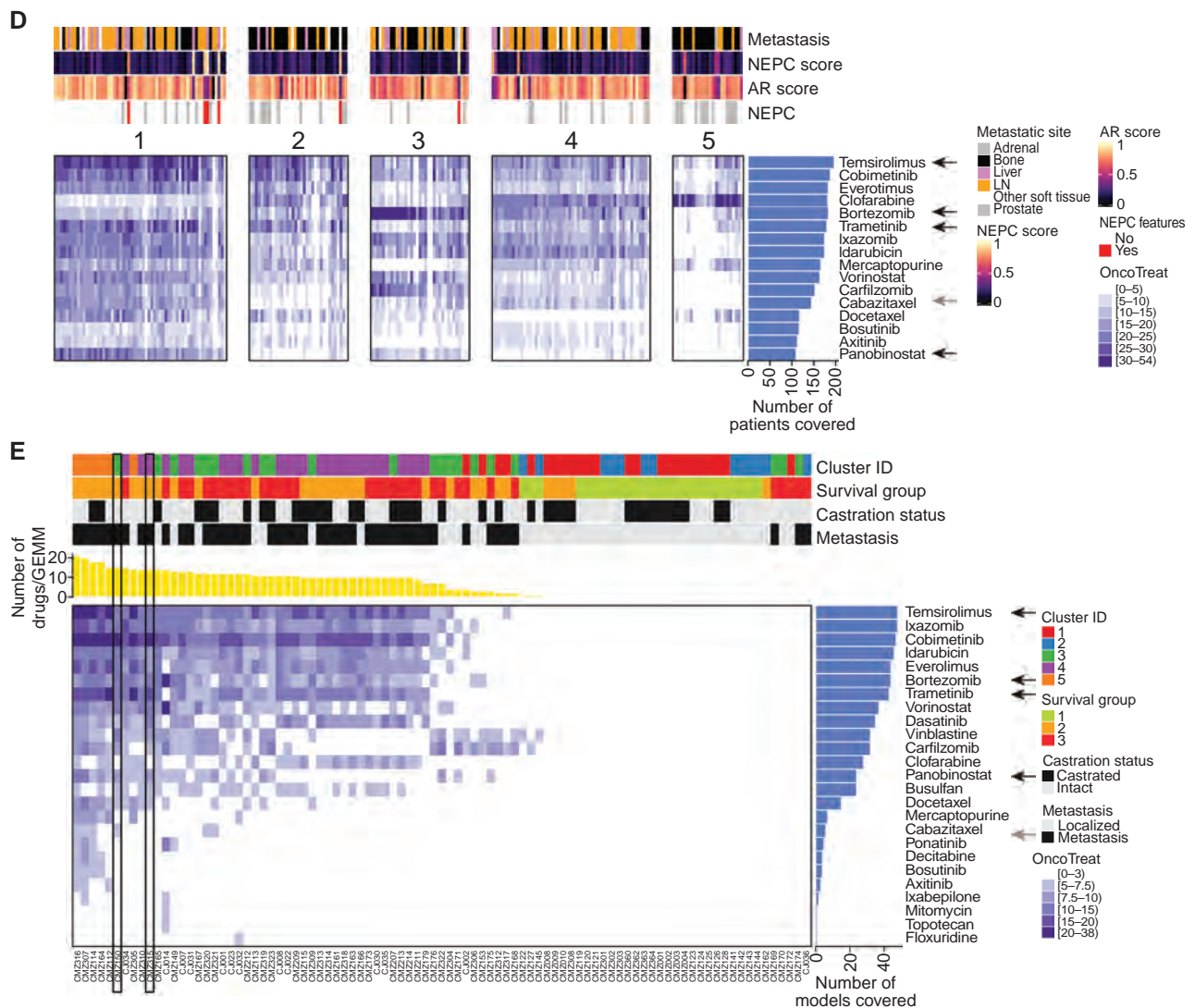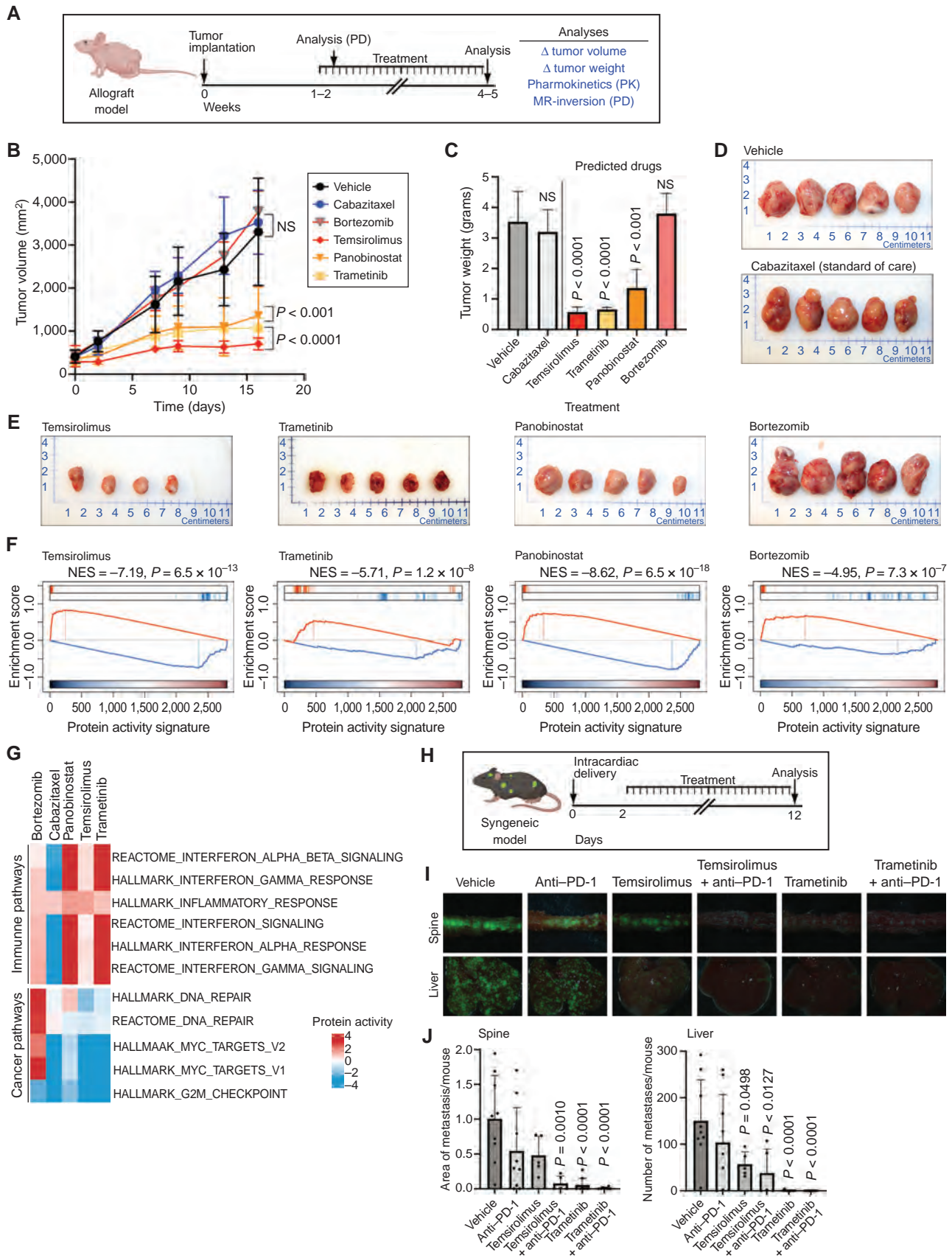
Figure 5. *(Continued)* **D** and **E,** Drug prioritization: FDA-approved drugs ($n = 117$; rows) were prioritized as candidate MR inverters of either patients from the SU2C cohort ($n = 212$; columns in **D**) or GEMM-DTs ($n = 91$; columns in **E**) using drug perturbation data from the DU145 cells. Drugs were filtered based on screened concentration ($\leq 1 \, \mu mol/L$) and patient coverage, that is, only those identified as MR inverters for >50% of the human samples are included. Relevant phenotypic variables for either patients or GEMM-DTs are shown in bars at the top of each heat map. The MR-inverter score ($-Log_{10}P$, as computed by aREA) is shown using a white ($P > 10^{-5}$) to dark blue heat map (see legend). The blue bar plots on the right summarize the number of patients or GEMM-DTs predicted as sensitive to each drug. Black arrows to their right point to candidate drugs selected for validation, whereas the gray arrows point to cabazitaxel, the standard-of-care for mCRPC. In **E**, the yellow bar plot at the top shows the number of drugs identified as significant MR inverters for each GEMM-DT and the rectangle indicates the allografts used for validation. See also Supplementary Tables S5 and S6 and Supplementary Figs. S7–S9. LN, lymph node.

bortezomib (proteosome inhibitor; NCT00193232 and NCT00183937). As a negative control, we selected cabazitaxel—a current standard of care for advanced prostate cancer that has variable efficacy in patients (8)—which was predicted as a significant MR-inverter for the human tumors but not for their cognate GEMM-DTs.

To test drug sensitivity predictions, we performed tumor growth assays in allografts derived from two cognate GEMM-DTs, namely, CMZ315 and CMZ150 (Fig. 6A–G; Supplementary Fig. S10A–S10F). These represent two of the aggressive GEMM clusters, C_3 and C_4, and were derived from p53-mutated and MYC-amplified mCRPC GEMM tumors, respectively (Supplementary Table S1). For each drug, we used their

published conditions for *in vivo* mouse studies to determine their appropriate concentration and treatment schedule, and we also confirmed their uptake into allograft tumors by pharmacokinetic assays (Supplementary Fig. S10A; see Supplementary Detailed Materials and Methods).

Three of the four predicted drugs—namely, temsirolimus, trametinib, and panobinostat—significantly reduced tumor volume and weight in allografts from both of the cognate GEMM-DTs ($P \leq 0.01$, one-way ANOVA; Fig. 6A–D; Supplementary Fig. S10C–S10F), whereas bortezomib emerged as a false positive because it did not significantly inhibit tumor growth in either allograft. Also consistent with predictions, cabazitaxel induced only modest tumor volume/weight

A Allograft model — Tumor implantation (0 Weeks) → Analysis (PD) (1–2) → Treatment → Analysis (4–5)

Analyses:
Δ tumor volume
Δ tumor weight
Pharmokinetics (PK)
MR-inversion (PD)

B Tumor volume (mm²) vs Time (days)
Vehicle, Cabazitaxel, Bortezomib, Temsirolimus, Panobinostat, Trametinib
NS
P < 0.001
P < 0.0001

C Tumor weight (grams) — Predicted drugs
Vehicle, Cabazitaxel (NS), Temsirolimus (P < 0.0001), Trametinib (P < 0.0001), Panobinostat (P < 0.001), Bortezomib (NS)
Treatment

D Vehicle
Cabazitaxel (standard of care)

E Temsirolimus, Trametinib, Panobinostat, Bortezomib

F
Temsirolimus NES = −7.19, P = 6.5 × 10⁻¹³
Trametinib NES = −5.71, P = 1.2 × 10⁻⁸
Panobinostat NES = −8.62, P = 6.5 × 10⁻¹⁸
Bortezomib NES = −4.95, P = 7.3 × 10⁻⁷
Enrichment score vs Protein activity signature

G
Bortezomib, Cabazitaxel, Panobinostat, Temsirolimus, Trametinib
Immune pathways:
REACTOME_INTERFERON_ALPHA_BETA_SIGNALING
HALLMARK_INTERFERON_GAMMA_RESPONSE
HALLMARK_INFLAMMATORY_RESPONSE
REACTOME_INTERFERON_SIGNALING
HALLMARK_INTERFERON_ALPHA_RESPONSE
REACTOME_INTERFERON_GAMMA_SIGNALING
Cancer pathways:
HALLMARK_DNA_REPAIR
REACTOME_DNA_REPAIR
HALLMAAK_MYC_TARGETS_V2
HALLMARK_MYC_TARGETS_V1
HALLMARK_G2M_CHECKPOINT
Protein activity 4 to −4

H Syngeneic model — Intracardiac delivery (0 Days) → (2) Treatment → Analysis (12)

I Vehicle, Anti–PD-1, Temsirolimus, Temsirolimus + anti–PD-1, Trametinib, Trametinib + anti–PD-1
Spine
Liver

J Spine — Area of metastasis/mouse
Vehicle, Anti–PD-1, Temsirolimus, Temsirolimus + anti–PD-1 (P = 0.0010), Trametinib (P < 0.0001), Trametinib + anti–PD-1 (P < 0.0001)

Liver — Number of metastases/mouse
Vehicle, Anti–PD-1, Temsirolimus (P = 0.0498), Temsirolimus + anti–PD-1 (P < 0.0127), Trametinib (P < 0.0001), Trametinib + anti–PD-1 (P < 0.0001)

reduction, which was borderline significant in only one of the two allografts. To ask whether these drugs produced a quantitatively different effect in models predicted to have higher versus lower sensitivity based on OncoLoop statistics, we assessed the effect of these same three drugs in an alternative p53-driven allograft (CMZ163) in which panobinostat was only borderline statistically significant (NES = 3.2) and temsirolimus and trametinib were predicted as the best (NES = 16.55) and second best (NES = 13.63) drugs, respectively (Supplementary Fig. S10B). Notably, tumor growth inhibition was highly consistent with the OncoLoop prediction statistics, with panobinostat showing a lower reduction in tumor volume compared with temsirolimus and trametinib (Supplementary Fig. S10G–S10I).

To better understand the effect of drugs on both MR activity and the activity of cancer-relevant pathways, we performed pharmacodynamic studies (Fig. 6F and G). First, we analyzed RNA-seq profiles of tumors following short-term (5-day) drug- versus vehicle control–treated CMZ315 allografts to assess MR-activity inversion before significant tumor cell death or necrosis could ensue. Confirming OncoLoop predictions, all four candidate drugs induced highly significant MR inversion *in vivo*, as evidenced by GSEA analyses showing significantly negative NES values ($P < 10^{-7}$, for all tested drugs, by one-tail aREA test; Fig. 6F). However, analysis of RNA-seq profiles from end-of-study samples showed that key cancer-related pathways were inverted only by the drugs that inhibited tumor growth—namely, temsirolimus, trametinib, and panobinostat—but not by those that failed to inhibit it—namely, bortezomib or cabazitaxel (Fig. 6G). Indeed, bortezomib was the only drug that, while inverting the MR-activity signature, also reprogrammed the tumors to a state with highly aberrant activity of MYC and DNA repair–related pathways (Fig. 6G).

Notably, in addition to cancer-related pathways, immune-related pathways were also significantly reactivated in tumors treated with predicted drugs compared with the vehicle control–treated animals, but not in cabazitaxel-treated animals (Fig. 6G). The effect was especially significant for panobinostat and trametinib, suggesting that these drugs may cooperate with immune-checkpoint inhibitors. Taken together, these findings (i) confirm that drugs predicted via OncoLoop to mediate MR inversion are frequently capable of abrogating tumor growth when experimentally validated *in vivo*, (ii) support the hypothesis that drug-mediated MR inversion is predictive of tumor growth inhibition, and (iii) suggest that treatment with predicted drugs can influence immune pathways, as previously reported (22).

Coclinical Validation in Clinically Relevant Contexts

Having demonstrated that OncoLoop predictions can be validated in cognate allograft tumor models *in vivo*, we next sought to validate the OncoLoop predictions in contexts that are more clinically relevant for human prostate cancer, namely, CRPC and metastasis. First, we asked whether OncoLoop-predicted drugs cooperate with the second-generation antiandrogen enzalutamide in hormone-sensitive and castration-resistant contexts (Supplementary Fig. S11A–S11G). Using the MR-matched CMZ315 GEMM-DT allograft (as above), we found that enzalutamide treatment increased rather than decreased tumor growth in castrated but not in intact mice ($P < 0.01$; Supplementary Fig. S11B and S11E), consistent with previous studies (34, 51). However, when combined with the predicted drug trametinib, enzalutamide treatment resulted in decreased rather than increased tumor growth in castrated mice ($P < 0.01$; compare Supplementary Fig. S11B–S11G). These findings suggest that OncoLoop predictions may enhance the efficacy of second-generation antiandrogens in patients with CRPC.

Second, we investigated the ability of the OncoLoop-predicted drugs to inhibit metastasis in immunocompetent mice. Toward this end, we used an MR-matched syngeneic cell model derived from a bone metastasis of an *NPK* GEMM (30) to test the ability of OncoLoop-predicted drugs to inhibit metastasis (Fig. 6H–J; Supplementary Fig. S10B). Notably, among the top-predicted drugs were trametinib and temsirolimus (Supplementary Fig. S10B), which also showed significant rescue of the negative immune- and inflammation-related pathway enrichment following treatment (see Fig. 6G). Given these observations and because this metastasis model is propagated in immunocompetent C57BL/6 mice, we evaluated the efficacy of these predicted drugs to inhibit metastasis both alone and in combination with the mouse equivalent of the PD-1 inhibitor nivolumab (Fig. 6H–J). Indeed, temsirolimus and trametinib significantly inhibited metastasis, both in bone (spine) and in soft tissues (liver; $P < 0.001$; Fig. 6I and J). Furthermore, although nivolumab alone was only modestly effective for inhibition of metastasis, its combination with either temsirolimus or trametinib yielded

Figure 6. Coclinical validation of OncoLoop-predicted drugs using GEMM-derived models. **A–G,** Validation in an allograft tumor model. **A,** Selected drugs were validated *in vivo* in allograft models derived from the cognate GEMM-DT CMZ315. Allografts were grown subcutaneously in nude mouse hosts, and the mice were treated with predicted drugs, vehicle control, and a negative control (cabazitaxel) for the times indicated. Following sacrifice, the tumors were collected and analyzed as indicated. (Created with BioRender.com.) **B,** Summary of tumor volume changes over the treatment period. **C,** Summary of tumor weights following sacrifice. *P* values for **B** and **C** were computed by one-way ANOVA at the last time point compared with vehicle-treated tumors and adjusted for multiple hypothesis testing with Dunnett test (10 animals were enrolled to the vehicle control arm and 5 animals were enrolled on each of the drug treatment arms). **D** and **E,** Representative images of final tumor sizes in vehicle control– and negative control–treated allografts (**D**) and allografts treated with predicted drugs (**E**). **F,** Pharmacodynamic assessment of MR inversion by GSEA for the four predicted drugs comparing drug- vs. vehicle-treated tumors. **G,** Enrichment analysis of selected immune- and cancer-related pathways based on the differential protein activity profiles between drug- and vehicle control–treated GEMM-DT CMZ315 allografts at the end of the study. **H–J,** Validation in a syngeneic metastasis model. **H,** Predicted drugs were validated *in vivo* for their effectiveness to inhibit metastasis using a syngeneic model. *NPK*^EYFP cells were delivered by intracardiac injection into immunocompetent mice, and drugs were administered individually and in combination with a PD-1 inhibitor. (Created with BioRender.com.) **I,** Representative images of spine and liver metastasis visualized by *ex vivo* fluorescence of YFP-expressing tumor cells for each experimental group. **J,** Quantification plots showing metastasis area (for spine) or metastases number (for liver) based on 2 independent experiments, each with *n* = 5 mice per group. *P* values were obtained by one-way ANOVA with Dunnett multiple comparisons against the vehicle. See also Supplementary Figs. S10 and S11. NS, not significant; PD, pharmacodynamics.

virtually no metastases in this model ($P < 0.0001$; Fig. 6I and J). These findings demonstrate OncoLoop's utility in predicting drugs likely to have an impact on the clinical care of patients with CRPC and mCRPC and are also consistent with our previous findings that MR-activity inversion contributes to modulating immune- and inflammation-related pathways (22).

Coclinical Validation in Cognate Human PDX Models

Lastly, to assess whether OncoLoop-predicted drugs were effective in a cognate human tumor context, we performed analogous coclinical studies using the well-characterized LuCaP series of PDX models, which were established from primary tumors and metastases obtained from the University of Washington Tissue Acquisition Necropsy program (15). Notably, the LuCaP PDX models were developed from biologically heterogeneous advanced prostate cancer tissues from primary and metastatic sites and include a range of tumors that vary in their response to castration, with some displaying castration sensitivity (15).

To identify cognate PDX models matched to the GEMM models used for drug predictions, we first generated RNA-seq profiles for five LuCaP PDX models that had been perturbed with multiple drugs and used these RNA-seq profiles to generate a PDX interactome (Supplementary Table S7A; see Supplementary Detailed Materials and Methods). Among all five baseline LuCaP PDX models, VIPER analysis identified LuCaP-73 as the most significantly matched to the GEMM-DTs used herein (Fig. 7A). Furthermore, among the candidate drugs identified for the human tumors (see Fig. 5D), several were identified as significant MR inverters for the LuCaP-73 PDX, including trametinib and panobinostat (Fig. 7B; Supplementary Fig. S10B; Supplementary Table S7B). We therefore tested whether these two drugs could abrogate LuCaP-73 viability *in vivo*. Indeed, both trametinib and panobinostat showed near-complete tumor growth inhibition ($P < 0.0001$; Fig. 7C–F). These findings provide further support for the translation of OncoLoop to a human prostate cancer context.

DISCUSSION

Predicting individualized drug efficacy in human patients remains a key challenge in precision medicine, and relatively few approaches have been described to identify models that best recapitulate patient-relevant drug response (6). To address these challenges, we have developed OncoLoop, which uses quantitative protein activity–based metrics to first identify high-fidelity and preexisting models for individual patient's tumors, then predict drug efficacy for a given patient's tumor and its cognate model, and lastly validate the drug predictions in the preexisting cognate model. In the current study, we demonstrate the effectiveness of OncoLoop in the context of prostate cancer. In particular, by leveraging an extensive and diverse collection of GEMMs, we find that >90% of patients with mCRPC in a published prostate cancer cohort are represented by at least one cognate GEMM-DT. We then use large-scale drug perturbation data from an MR-matched prostate cancer cell line to predict MR-inverter drugs for the patients and their cognate models. The

predicted MR-inverter drugs were experimentally validated in allografts from the GEMM-DT series, in a syngeneic model of metastasis, and in a PDX model of human prostate cancer. Notably, OncoLoop-predicted drugs enhanced the efficacy of clinically relevant drugs in both castration-resistant and metastatic contexts. These results suggest that OncoLoop could be a useful methodology to evaluate candidate drugs for clinical trials, including umbrella and basket trials, based on *in vivo* validated drug stratification across models representing distinct pharmacotypes (Fig. 7G). In addition, OncoLoop provides an accurate and versatile framework for both predicting and evaluating individualized drug treatments in real time. Notably, because all of the resources described herein are available to the research community, OncoLoop could be readily applied to prostate cancer in clinical practice.

Beyond prostate cancer, OncoLoop is readily generalizable for predicting both cognate models and drug sensitivity for other cancers, as well as in noncancer-related contexts. Notably, large-scale human, GEMM, and/or PDX cohorts are now available for many cancer types. In addition, we have already generated genome-wide perturbational profiles in cell lines, comprising representatives for 23 distinct tumor subtypes (see ref. 27 for partial coverage of the PanACEA database). Critically, the ability to stratify drug sensitivity in precisely identified molecular subtypes (pharmacotypes), if further validated, may lead to rapid design of basket and umbrella trials, including using adaptive design approaches to efficiently replace baskets that fail to validate.

Nonetheless, there are also several caveats that will benefit from further refinements. First, despite the benefit of using FDA-approved drugs for rapid translation to clinical practice, the downside of focusing only on drugs that are FDA approved or in phase II/III trials, is that such drugs may not be optimal for targeting the MR proteins most relevant for the tumors. Therefore, in future studies, extension to additional experimental agents may expand the repertoire of effective drugs, especially considering the new classes of proteolysis-targeting chimeras (52) and antisense agents (53). Furthermore, we note that the drugs tested in these studies in mice are not pharmaceutical grade as would be used in humans, which represents a potential limitation of the work. Additionally, drug perturbation profiles are limited by the availability of appropriate cell lines MR-matched to human patients. For example, the current study does not adequately inform on drugs that target NEPC tumors because neither the LNCaP nor the DU145 cell line recapitulates the MR-activity signature of this subtype. This could be addressed in future studies by generating drug perturbation profiles from primary, NEPC patient-derived cells or organoids. Similarly, the focus of the current studies is on predicting drugs that target the tumor rather than stromal or immune cells, which could also be addressed in future studies using appropriate drug perturbation analyses, as shown for instance for T regulatory cells (54).

Moreover, despite the encouraging results reported here, MR signature analysis and MR-inverter drug predictions are not 100% accurate, as is the case for most machine learning methods. This can depend on multiple causes. For instance, MR-activity inversion may lead to multiple distinct cell states, some of which may still be oncogenic and viable, as shown for bortezomib. In addition, as drug prioritization is based
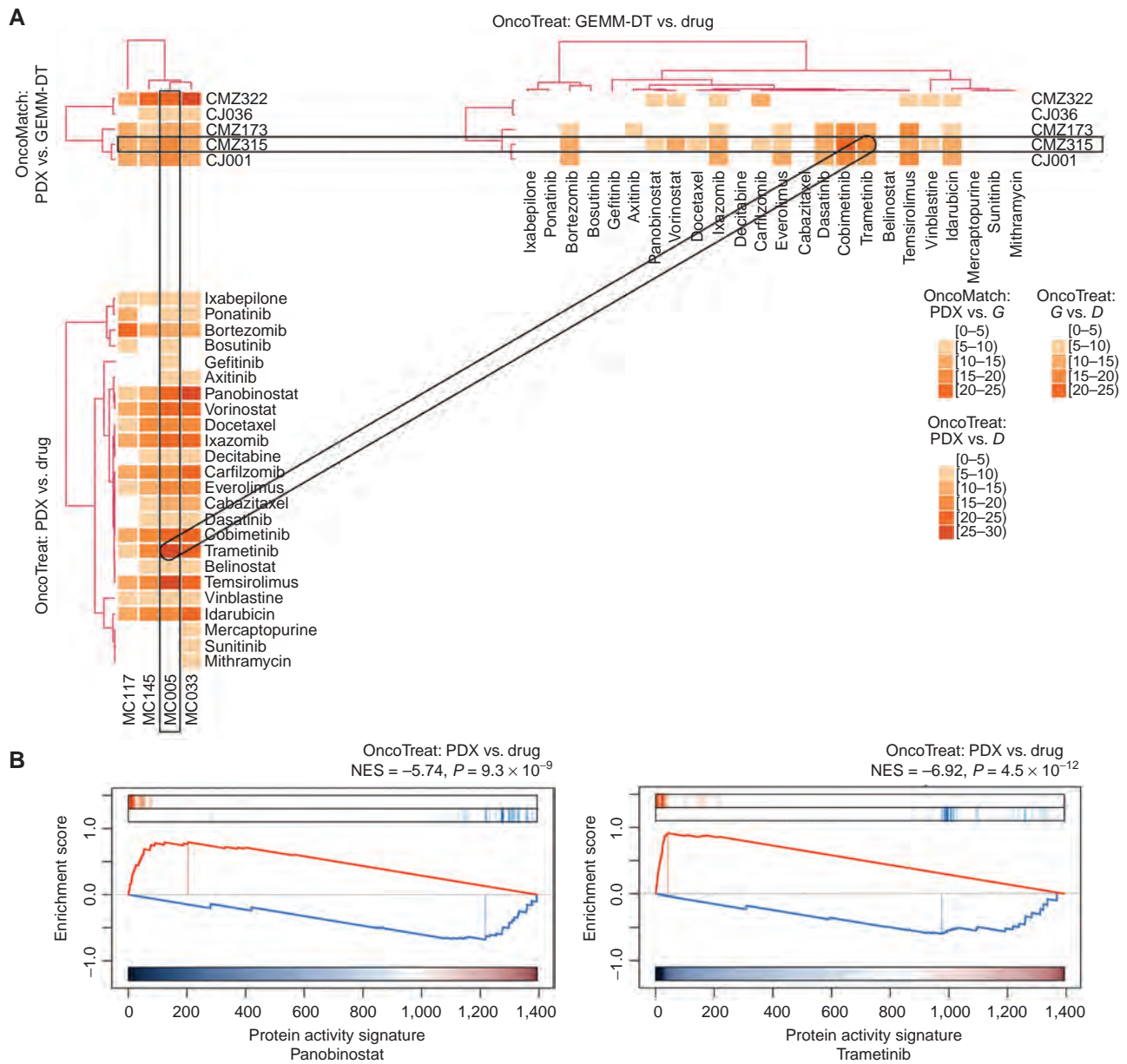
Figure 7. Coclinical validation of OncoLoop-predicted drugs using a human PDX model. **A** and **B,** OncoLoop analysis of PDX models. **A,** Similar to Fig. 5A, three heat maps are shown, representing the fidelity and MR-inverter scores for four LuCaP PDX tumors (columns in left heat maps), five GEMM-DTs, and 28 drugs. The rectangles show a representative PGD-loop comprising a PDX (MC005/LuCaP-73), its cognate GEMM-DT (CMZ315), and two of the top-predicted drug candidates evaluated in the allograft models (panobinostat and trametinib). For visualization purposes, heat maps were clustered as in Fig. 5A. **B,** GSEA was used to compute panobinostat's and trametinib's MR-inverter P values for the MC005/LuCaP-73 model. (*continued on next page*)

on overall MR-inversion signature, the effect of MRs that are more likely to elicit essentiality is not directly accounted for.

Another key caveat is the largely heterogeneous nature of most tumors, which present molecularly distinct subpopulations with potentially equally distinct drug sensitivity. Thus, when used to analyze bulk tumor profiles, OncoLoop may miss the opportunity to nominate drugs targeting the less represented subpopulations, thus selecting for drug-resistant ones and ultimately leading to relapse. A possible way to overcome this is to perform OncoLoop analyses at the single-cell level, which should enable the prioritization of drugs

for all detectable subpopulations (55). A second approach is to perform analysis on the posttreatment minimal residual tumor mass, which is likely highly enriched for resistant subpopulations (56, 57). Additionally, while OncoLoop predictions are transcriptome-based, recent results show that additional omics modalities, such as a patient's mutational profile and protein structure, among others, can be readily integrated to further refine MR protein identification and drug prediction (22).

Beyond cancer, MR-based predictions have been validated in diseases as different as Parkinson's (58), amyotrophic
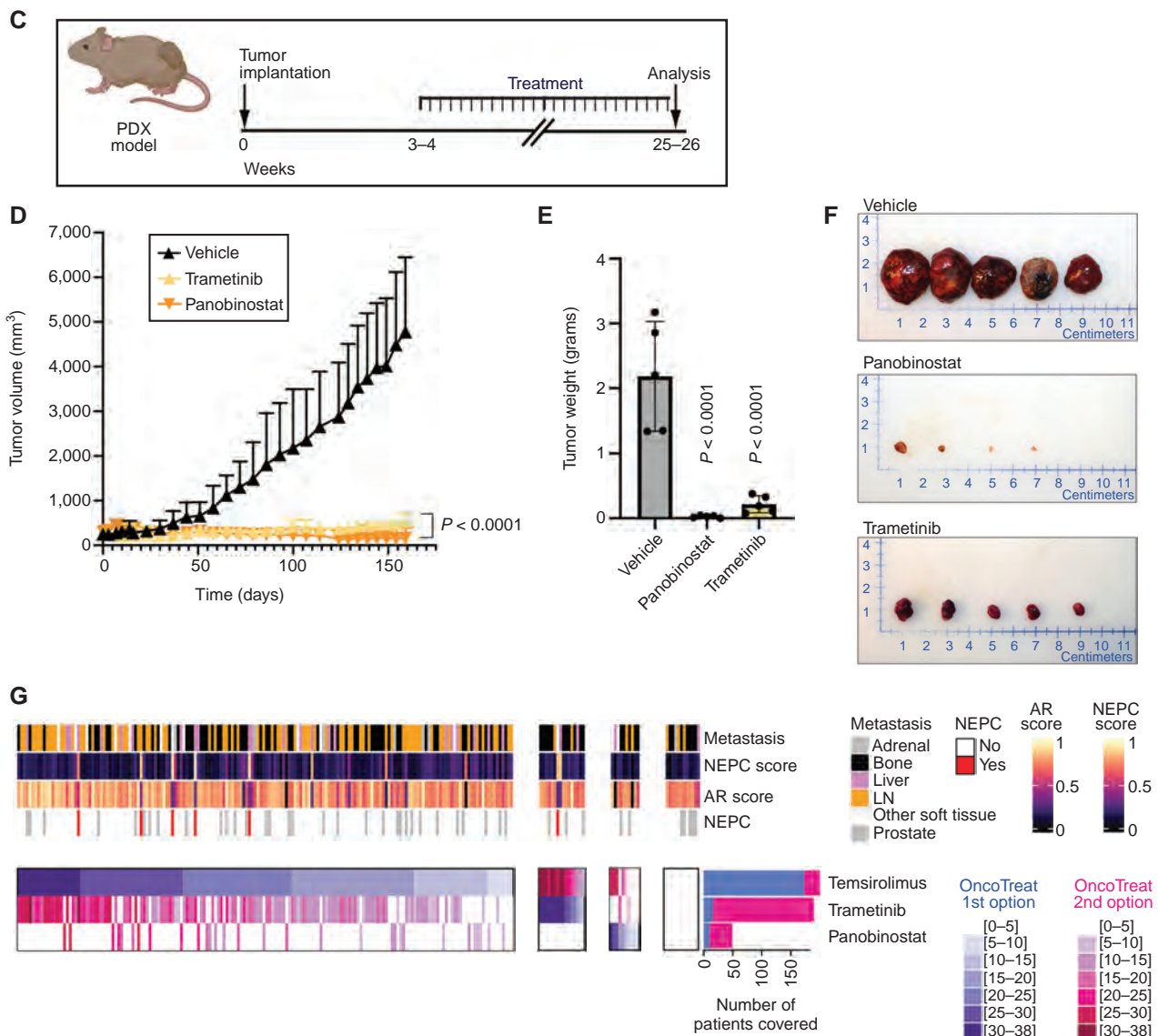
Figure 7. *(Continued)* **C–F,** Validation in the PDX model. **C,** The MC005/LuCaP-73 PDX was grown in nude mouse hosts and treated with predicted drugs or vehicle for the times indicated. (Created with BioRender.com.) **D,** Summary of changes in tumor volume over the treatment period. **E,** Summary of tumor weights following sacrifice. *P* values for **C** and **D** were computed by one-way ANOVA at the last time point compared with vehicle control–treated models and adjusted for multiple hypothesis testing with Dunnett test. **F,** Representative images of final tumor sizes. **G,** Pharmacotype analysis: Identification of patient subsets predicted to be sensitive to the same drugs by cluster analysis. Four subtypes are identified, including patients with the highest predicted sensitivity to temsirolimus, trametinib, and panobinostat, as well as patients for whom none of the three drugs was statistically significant. For each patient, the score of the most statistically significant MR-inverter drug is shown using a white (nonsignificant) to dark blue color map (see legend); the second most significant drug is shown using a white (nonsignificant) to dark red color map (see legend). This heat map provides the rationale for a possible umbrella or combination trial where each patient (column) could be randomized to the most statistically significant MR-inverter drug (rows) validated in the preclinical study, based on its MR-inversion score, or to the combination of the two most significant drugs. The bar plots to the right show the total number of patients predicted to be sensitive to each drug as either most significant (blue) or second best selection (red). See also Supplementary Table S7. LN, lymph node.

lateral sclerosis (59), alcohol dependency (60), and type II diabetes (61), suggesting direct OncoLoop applicability to such contexts, as long as appropriate drug perturbation data are available. Indeed, although human translation of drugs validated in a GEMM or PDX context has been reasonably effective in cancer, mouse models have largely failed to recapitulate the effect of drugs on human disease. In this context, OncoLoop's quantitative fidelity metrics may help to identify more appropriate mouse models for drug validation.

The current design of OncoLoop relies on MR-based predictions of model similarity and drug sensitivity. However, alternative approaches could also be tested using the same framework presented here. For instance, transcriptome-based approaches have shown promising results in predicting the sensitivity of human patients in a clinical context (62), whereas neural network–based methods trained on multiomics data have shown promising results in translating drug sensitivity assays from a training set of cell lines and mouse models to an

independent test set of PDX models (63). Similarly, transcriptome-based approaches for assessing model fidelity have also been proposed (64).

Taken together, our data show that OncoLoop may provide a valuable contribution to the emergent field of precision medicine by complementing rather than supplanting existing approaches based on its ability to couple effective drug and high-fidelity model predictions.

METHODS

GEMMs of Prostate Cancer

All experiments using animals were performed according to protocols approved by the Institutional Animal Care and Use Committee (IACUC) at Columbia University Irving Medical Center (CUIMC). The GEMMs in this study utilize the *Nkx3.1*[CreERT2/+] allele to activate an inducible Cre recombinase in the prostatic epithelium (35). The *Nkx3.1*[CreERT2/+] allele was crossed with various other mouse alleles to achieve conditional deletion or conditional activation in the prostatic epithelium or with the Hi-Myc transgene (39). For lineage tracing, mice were further crossed with a conditionally activatable fluorescent reporter allele (*Rosa-CAG-LSL-EYFP-WPRE*; ref. 42). All mice were maintained on a mixed strain, predominantly C57BL/6 background. Since the focus of our study is prostate cancer, only male mice were used. All multiallelic strains are available from The Jackson Laboratory (Supplementary Table S1A). Mice were induced to form tumors at 2 to 3 months of age by administration of 100 mg/kg tamoxifen (Sigma-Aldrich T5648) in corn oil; control mice received corn oil alone. After tamoxifen induction, mice were monitored 3 times weekly and euthanized when their body condition score was <1.5, or when they experienced body weight loss ≥20% or signs of distress, such as difficulty breathing or bladder obstruction. Surgical castration was performed at 1 to 10 months after tumor induction (Supplementary Table S1A). Tumor volume was monitored by MRI using a Bruker 9.4T Biospec Biospec Magnetic Resonance Imager (RRID:SCR_018054). Volumetric analysis was done using 3DSlicer software (http://www.slicer.org; RRID:SCR_005619).

At the time of sacrifice, tissues were collected and YFP-positive prostatic tumors and metastases were visualized by *ex vivo* fluorescence using an Olympus SZX16 microscope (Ex 490–500/Em 510–560 filter). For histopathologic analysis, tissues were fixed in 10% formalin (Fisher Scientific), and hematoxylin and eosin and immunostaining were done using 3-μm paraffin sections as described (30, 34). Histopathologic scoring of GEMM prostate cancer phenotypes is summarized in Supplementary Table S1A and S1B.

Following protocols approved by IACUC at CUIMC, allografts were generated by transplanting freshly dissected prostate tissues from the GEMMs subcutaneously into the flank of male athymic nude mice (Hsd:Athymic Nude-Foxn1nu, Envigo; RRID:MGI:5652489). Allografted tumors were harvested when their size reached 2 cm or earlier if the body condition score of the host mouse was <1.5 or the mice exhibited signs of distress. A summary of allografted tumors is provided in Supplementary Table S1A. Mouse tumor organoids were generated as described (65). A summary of organoids is provided in Supplementary Table S1A. A syngeneic model of metastasis was adapted from a previously established cell line from the prostate cancer bone metastasis of intact *NPK*[EYFP] mice (30).

Transcriptomic Analysis of GEMMs

RNA-seq data were generated from 136 GEMM-DTs or GEMM-derived normal prostate (Supplementary Table S2A). RNA was prepared by homogenization in TRIzol Reagent (Invitrogen), and total RNA was enriched for mRNA using poly-A pulldown. Samples were sequenced using an Illumina HiSeq 2500/4000 or NovaSeq 6000, and

RNA-seq profiles were mapped to the mouse reference genome (version GRCm38 mm10). A GEMM prostate cancer–specific regulatory network (interactome) was reverse engineered from the resulting 136 RNA-seq profiles using ARACNe (29).

Subsequent analyses focused on a subset of 91 GEMM-DTs that recapitulated pathophysiologically relevant prostate cancer phenotypes (Supplementary Table S1B). The VIPER algorithm (23) was used to transform RNA-seq profiles of each GEMM-DT into differential protein activity profiles. The resulting regulatory network, comprising regulons of 2,794 regulatory proteins, is summarized in Supplementary Table S2B.

PDX Model Analysis

Following protocols approved by IACUC at CUIMC, LuCaP PDX lines 73, 77, 78, 81, and 147 (15) were continuously maintained by a passage in male CIEA NOG mice (Taconic; RRID:IMSR_TAC:HSCFTL-NOG). Xenografts were harvested when the tumor size reached 2 cm or earlier if the body condition score of the host mice was <1.5 or if they exhibited signs of distress. When the Xenograft tumors were 7 to 8 mm in diameter, the host mice were castrated or left intact (mock surgery). Three days later, the mice were treated with either vehicle or one of 13 selected perturbagens, as described in ref. 20. On the afternoon of the fifth day of treatment, mice were euthanized and tumors were collected and snap-frozen in liquid nitrogen for a total of 140 samples (five models, 14 treatments, and two castration states). RNA-seq profiles were obtained as described above for the GEMM-DT cohort. A xenograft interactome was generated from the 120 highest quality xenograft-derived RNA-seq profiles, as described for the GEMM cohort. Results are provided in Supplementary Table S7A.

Human Patient Cohort Analysis

For the analysis of human prostate cancer tumors and normal prostate, we collected $n = 790$ RNA-seq profiles from published sources, including profiles from (i) 245 normal prostate tissues from the GTEx consortium (version 8, date 2017-06-05; ref. 47); (ii) 333 treatment-naïve, clinically annotated primary prostate adenocarcinoma samples in TCGA (25); and (iii) 212 metastatic biopsies from the SU2C cohort (26). The primary prostate tumor interactome was generated using the full set of 498 patients in the TCGA prostate cancer cohort (25); data are provided in Supplementary Table S3A. The SU2C interactome was generated using 212 patients for which RNA-seq data are available; data are provided in Supplementary Table S3B. Differential protein activity was measured by VIPER analysis; protein activity profiles are provided in Supplementary Tables S3C and S3D.

OncoMatch Analysis

For this analysis, we used protein activity signatures from individual GEMM-DT or PDX tumors to compute the NES of the 25↑+25↓ most differentially active proteins, as assessed by VIPER, as in ref. 24. The aREA algorithm (23) was used to estimate NES that were converted to P values. The conservative Bonferroni method was used to correct for multiple hypothesis testing, and the value $S_F = -\text{Log}_{10}P$ was used as an MR conservation-based fidelity score. Results for all TCGA and SU2C cohort samples are provided in Supplementary Table S4A and S4B, respectively.

Drug Perturbation Analyses

LNCaP (RRID:CVCL_0395) and DU145 (RRID:CVCL_0105) human prostate cancer cells were obtained from the ATCC, which verifies their authenticity. Cells were maintained under *Mycoplasma*-free conditions, and only low passage cells were used. These cell lines were identified as the pair with the optimal joint coverage of TCGA and SU2C cohorts ($P \leq 10^{-5}$) and were thus selected for drug perturbation assays. For drug perturbation analyses, the maximum sublethal

concentration (defined as its 48-hour EC_{20} concentration) was first defined for each drug. Following this, cells were seeded onto 384-well tissue culture plates, and approximately 12 hours later, compounds were added at their EC_{20}. Cells were harvested 24 hours after perturbation and subject to PLATE-seq analyses (48). The drug perturbation data are provided in Supplementary Table S5B.

OncoTreat Analysis

This analysis was performed as described in ref. 21. Briefly, drug-mediated MR inversion was independently assessed for each patient in the SU2C cohort and each GEMM as follows by assessing the NES of the sample's MR-activity signature (25↑+25↓ most differentially active proteins). NES values were converted to P values and Bonferroni corrected to account for multiple hypothesis testing. An efficacy score was computed $S_E = -\text{Log}_{10}P$ and used to identify MR-inverter drugs ($S_E \geq 5$, corresponding to $P \leq 10^{-5}$). Results of OncoTreat analyses for the SU2C and GEMM cohorts are provided in Supplementary Table S5C and S5D, respectively.

OncoLoop Analysis

The OncoLoop algorithm leverages a tripartite graph, TPG, with nodes representing patients (P_i), GEMM-DT (G_j) and drugs (D_k), respectively, and edges represent statistically significant GEMM–patient fidelity score $S_M(P_i, j_j) \geq 5$ ($P \leq 10^{-5}$), GEMM–drug MR-inverter score $S_E(G_j, D_k) \geq 5$ ($P \leq 10^{-5}$), and patient–drug MR-inverter score $S_E(P_i, D_k) \geq 5$ ($P \leq 10^{-5}$). All closed 3-node loops including a patient, a GEMM-DT, and a drug are considered statistically significant PGD-loops. These are then ranked based on the Stouffer integration of the z-scores corresponding to the $S_M(P_i, G_j)$, $S_E(G_j, D_k)$, and $S_E(P_i, D_k)$ values of the loop, which can then be converted back to a P value. Results are summarized in Supplementary Table S6.

Preclinical Validation of OncoLoop-Predicted Drugs

Following protocols approved by IACUC at CUIMC, allograft models ($NPp53^{mut}$ CMZ315, $NPp53^{mut}$ CMZ163, and NPM CMZ150) were grown in the flanks of male athymic nude mice (Hsd:Athymic Nude-Foxn1nu, Envigo; RRID:MGI:5652489). The LuCaP-73 PDX was grown in R2G2 mice (B6;129-Rag2^{tm1Fwa}II2rg^{tm1Rsky}/DwlHsd, Envigo, RRID:IMSR_ENV:HSD-021). Tumors were monitored by caliper measurement twice weekly, and tumor volumes were calculated using the formula [Volume = (width)^2 × length/2]. When tumors reached 100 to 200 mm^3, mice with similar mean tumor volume were randomized into vehicle and treatment groups. For the syngeneic metastasis model, NPK^{EYFP} cells (1×10^5) were injected into the left heart ventricle of C57BL/6 male mice (The Jackson Laboratory; cat. #000664, RRID:IMSR_JAX:000664). Two days after the intracardiac injection, mice were randomly assigned to the vehicle and treatment groups.

Pharmaceutical-grade (99% purity) compounds, namely, temsirolimus (S1044), trametinib (S2673), panobinostat (S1030), bortezomib (S1013), cabazitaxel (S3022), and enzalutamide (S1250), were purchased from Sellekchem. The monoclonal antibody anti–PD-1 (BE0146, RRID:AB_10949053) and the corresponding rat IgG2a antitrinitrophenol isotype control (BE0089, RRID:AB_1107769) were purchased from Bio X Cell. For each drug, the dosage, mode of delivery, and schedule were chosen based on previous reports as follows: enzalutamide (10 mg/kg; ref. 66), temsirolimus (20 mg/kg; ref. 67), trametinib (1 mg/kg; ref. 68), panobinostat (15 mg/kg; ref. 69), bortezomib (1 mg/kg; ref. 70), cabazitaxel (10 mg/kg; ref. 71), and anti–PD-1 (10 mg/kg; ref. 72). Drugs were administered via intraperitoneal delivery 3 times/week in nonconsecutive days (temsirolimus, panobinostat, bortezomib, and cabazitaxel) or every 72 hours (anti–PD-1), or by oral gavage 5 times/week in consecutive days (trametinib and enzalutamide). Tumors were harvested when the tumor size of vehicle-treated mice reached 2 cm or earlier if the

body condition score of the host mice was <1.5 or if they exhibited signs of distress. Tumors were fixed in 10% formalin to be processed for histology or snap-frozen in liquid nitrogen. For the syngeneic metastasis model, mice were euthanized 12 days after intracardiac injection, and metastasis was analyzed by *ex vivo* fluorescence (30).

Statistical Analyses

Statistical analysis was performed using GraphPad Prism software (Version 9.3.1; RRID:SCR_002798) and R-studio (0.99.902, R v4.0.2; RRID:SCR_000432). Kaplan–Meier survival analysis was performed using a two-tailed log-rank test compared with the NP model. Comparison of frequencies was done using a two-tailed Fisher exact test or as described in figure legends. Subcutaneous tumor growth curves were analyzed using one-way ANOVA at the last time point compared with vehicle-treated tumors and adjusted for multiple comparisons with the Dunnett test. Metastasis was analyzed using one-way ANOVA compared with vehicle-treated group and adjusted for multiple comparisons with the Dunnett test. All bars show the mean and error bars the SD. No statistical method was used to predetermine the sample size used for *in vivo* experiments.

Data Accession

The following datasets are deposited in the Gene Expression Omnibus (GEO): (i) the mouse gene expression profiles (raw and normalized data; GSE186566); (ii) the human PDX gene expression profiles (raw and normalized data; GSE184427); and (iii) the PLATE-seq data for the drug perturbation profiles in both LNCaP and DU145 cells (GEO199800).

Complete details of all materials and methods are provided in the Supplementary Materials.

Authors' Disclosures

Authors' Contributions

A. Vasciaveo: Conceptualization, data curation, software, formal analysis, investigation, visualization, methodology, writing–original draft, writing–review and editing. **J.M. Arriaga:** Conceptualization, data curation, formal analysis, investigation, methodology, writing–original draft, writing–review and editing. **F. Nunes de Almeida:** Conceptualization, data curation, formal analysis, investigation, methodology, writing–original draft, writing–review and editing. **M. Zou:** Conceptualization, data curation, formal analysis, investigation, methodology, writing–review and editing. **E.F. Douglass Jr:** Data curation, formal analysis, methodology, writing–review and editing. **F. Picech:** Conceptualization, data curation, formal analysis, investigation, visualization, methodology, writing–review and editing. **M. Shibata:** Data curation, formal analysis, investigation, methodology, writing–original draft, writing–review and editing. **A. Rodriguez-Calero:** Formal analysis, investigation, writing–review

REFERENCES

1. Mattar M, McCarthy CR, Kulick AR, Qeriqi B, Guzman S, de Stanchina E. Establishing and maintaining an extensive library of patient-derived xenograft models. Front Oncol 2018;8:19.
2. Tentler JJ, Tan AC, Weekes CD, Jimeno A, Leong S, Pitts TM, et al. Patient-derived tumour xenografts as models for oncology drug development. Nat Rev Clin Oncol 2012;9:338–50.
3. Bleijs M, van de Wetering M, Clevers H, Drost J. Xenograft and organoid model systems in cancer research. EMBO J 2019;38:e101654.
4. Schutgens F, Clevers H. Human organoids: tools for understanding biology and treating diseases. Annu Rev Pathol 2020;15:211–34.
5. Kersten K, de Visser KE, van Miltenburg MH, Jonkers J. Genetically engineered mouse models in oncology research and cancer medicine. EMBO Mol Med 2017;9:137–53.
6. Usary J, Zhao W, Darr D, Roberts PJ, Liu M, Balletta L, et al. Predicting drug responsiveness in human cancers using genetically engineered mice. Clin Cancer Res 2013;19:4889–99.
7. Siegel RL, Miller KD, Fuchs HE, Jemal A. Cancer statistics, 2021. CA Cancer J Clin 2021;71:7–33.
8. Sartor O, de Bono JS. Metastatic prostate cancer. N Engl J Med 2018;378:645–57.
9. Scher HI, Sawyers CL. Biology of progressive, castration-resistant prostate cancer: directed therapies targeting the androgen-receptor signaling axis. J Clin Oncol 2005;23:8253–61.
10. Watson PA, Arora VK, Sawyers CL. Emerging mechanisms of resistance to androgen receptor inhibitors in prostate cancer. Nat Rev Cancer 2015;15:701–11.
11. Beltran H, Prandi D, Mosquera JM, Benelli M, Puca L, Cyrta J, et al. Divergent clonal evolution of castration-resistant neuroendocrine prostate cancer. Nat Med 2016;22:298–305.
12. Rickman DS, Beltran H, Demichelis F, Rubin MA. Biology and evolution of poorly differentiated neuroendocrine tumors. Nat Med 2017;23:1–10.
13. Armenia J, Wankowicz SAM, Liu D, Gao J, Kundra R, Reznik E, et al. The long tail of oncogenic drivers in prostate cancer. Nat Genet 2018;50:645–51.
14. Arriaga JM, Abate-Shen C. Genetically engineered mouse models of prostate cancer in the postgenomic era. Cold Spring Harb Perspect Med 2019;9:a030528.
15. Nguyen HM, Vessella RL, Morrissey C, Brown LG, Coleman IM, Higano CS, et al. LuCaP prostate cancer patient-derived xenografts reflect the molecular heterogeneity of advanced disease and serve as models for evaluating cancer therapeutics. Prostate 2017;77:654–71.
16. Gao D, Vela I, Sboner A, Iaquinta PJ, Karthaus WR, Gopalan A, et al. Organoid cultures derived from patients with advanced prostate cancer. Cell 2014;159:176–87.
17. Puca L, Bareja R, Prandi D, Shaw R, Benelli M, Karthaus WR, et al. Patient-derived organoids to model rare prostate cancer phenotypes. Nat Commun 2018;9:2404.
18. Karkampouna S, La Manna F, Benjak A, Kiener M, De Menna M, Zoni E, et al. Patient-derived xenografts and organoids model therapy response in prostate cancer. Nat Commun 2021;12:1117.
19. Servant R, Garioni M, Vlajnic T, Blind M, Pueschel H, Muller DC, et al. Prostate cancer patient-derived organoids: detailed outcome from a prospective cohort of 81 clinical specimens. J Pathol 2021;254:543–55.

20. Aytes A, Mitrofanova A, Lefebvre C, Alvarez MJ, Castillo-Martin M, Zheng T, et al. Cross-species regulatory network analysis identifies a synergistic interaction between FOXM1 and CENPF that drives prostate cancer malignancy. Cancer Cell 2014;25:638–51.

21. Alvarez MJ, Subramaniam PS, Tang LH, Grunn A, Aburi M, Rieckhof G, et al. A precision oncology approach to the pharmacological targeting of mechanistic dependencies in neuroendocrine tumors. Nat Genet 2018;50:979–89.

22. Paull EO, Aytes A, Jones SJ, Subramaniam PS, Giorgi FM, Douglass EF, et al. A modular master regulator landscape controls cancer transcriptional identity. Cell 2021;184:334–51.

23. Alvarez MJ, Shen Y, Giorgi FM, Lachmann A, Ding BB, Ye BH, et al. Functional characterization of somatic mutations in cancer using network-based inference of protein activity. Nat Genet 2016;48:838–47.

24. Alvarez MJ, Yan P, Alpaugh ML, Bowden M, Sicinska E, Zhou CW, et al. Reply to 'H-STS, L-STS and KRJ-I are not authentic GEPNET cell lines'. Nat Genet 2019;51:1427–8.

25. Cancer Genome Atlas Research N. The molecular taxonomy of primary prostate cancer. Cell 2015;163:1011–25.

26. Abida W, Cyrta J, Heller G, Prandi D, Armenia J, Coleman I, et al. Genomic correlates of clinical outcome in advanced prostate cancer. Proc Natl Acad Sci U S A 2019;116:11428–36.

27. Douglass EF Jr, Allaway RJ, Szalai B, Wang W, Tian T, Fernandez-Torras A, et al. A community challenge for a pancancer drug mechanism of action inference from perturbational profile data. Cell Rep Med 2022;3:100492.

28. Obradovic A, Chowdhury N, Haake SM, Ager C, Wang V, Vlahos L, et al. Single-cell protein activity analysis identifies recurrence-associated renal tumor macrophages. Cell 2021;184:2988–3005.

29. Basso K, Margolin AA, Stolovitzky G, Klein U, Dalla-Favera R, Califano A. Reverse engineering of regulatory networks in human B cells. Nat Genet 2005;37:382–90.

30. Arriaga JM, Panja S, Alshalalfa M, Zhao J, Zou M, Giacobbe A, et al. A MYC and RAS co-activation signature in localized prostate cancer drives bone metastasis and castration resistance. Nat Cancer 2020;1:1082–96.

31. Aytes A, Mitrofanova A, Kinkade CW, Lefebvre C, Lei M, Phelan V, et al. ETV4 promotes metastasis in response to activation of PI3-kinase and Ras signaling in a mouse model of advanced prostate cancer. Proc Natl Acad Sci U S A 2013;110:E3506–15.

32. Floc'h N, Kinkade CW, Kobayashi T, Aytes A, Lefebvre C, Mitrofanova A, et al. Dual targeting of the Akt/mTOR signaling pathway inhibits castration-resistant prostate cancer in a genetically engineered mouse model. Cancer Res 2012;72:4483–93.

33. Wang J, Kobayashi T, Floc'h N, Kinkade CW, Aytes A, Dankort D, et al. B-Raf activation cooperates with PTEN loss to drive c-Myc expression in advanced prostate cancer. Cancer Res 2012;72:4765–76.

34. Zou M, Toivanen R, Mitrofanova A, Floch N, Hayati S, Sun Y, et al. Transdifferentiation as a mechanism of treatment resistance in a mouse model of castration-resistant prostate cancer. Cancer Discov 2017;7:736–49.

35. Wang X, Kruithof-de Julio M, Economides KD, Walker D, Yu H, Halili MV, et al. A luminal epithelial stem cell that is a cell of origin for prostate cancer. Nature 2009;461:495–500.

36. Lesche R, Groszer M, Gao J, Wang Y, Messing A, Sun H, et al. Cre/loxP-mediated inactivation of the murine Pten tumor suppressor gene. Genesis 2002;32:148–9.

37. Chen Y, Chi P, Rockowitz S, Iaquinta PJ, Shamu T, Shukla S, et al. ETS factors reprogram the androgen receptor cistrome and prime prostate tumorigenesis in response to PTEN loss. Nat Med 2013;19:1023–9.

38. Olive KP, Tuveson DA, Ruhe ZC, Yin B, Willis NA, Bronson RT, et al. Mutant p53 gain of function in two mouse models of Li-Fraumeni syndrome. Cell 2004;119:847–60.

39. Ellwood-Yen K, Graeber TG, Wongvipat J, Iruela-Arispe ML, Zhang J, Matusik R, et al. Myc-driven murine prostate cancer shares molecular features with human prostate tumors. Cancer Cell 2003;4:223–38.

40. Dankort D, Filenova E, Collado M, Serrano M, Jones K, McMahon M. A new mouse model to explore the initiation, progression, and therapy of BRAFV600E-induced lung tumors. Genes Dev 2007;21:379–84.

41. Jackson EL, Willis N, Mercer K, Bronson RT, Crowley D, Montoya R, et al. Analysis of lung tumor initiation and progression using conditional expression of oncogenic K-ras. Genes Dev 2001;15:3243–8.

42. Madisen L, Zwingman TA, Sunkin SM, Oh SW, Zariwala HA, Gu H, et al. A robust and high-throughput Cre reporting and characterization system for the whole mouse brain. Nat Neurosci 2010;13:133–40.

43. Shen MM, Abate-Shen C. Molecular genetics of prostate cancer: new prospects for old challenges. Genes Dev 2010;24:1967–2000.

44. Aytes A, Giacobbe A, Mitrofanova A, Ruggero K, Cyrta J, Arriaga J, et al. NSD2 is a conserved driver of metastatic prostate cancer progression. Nat Commun 2018;9:5201.

45. Arora VK, Schenkein E, Murali R, Subudhi SK, Wongvipat J, Balbas MD, et al. Glucocorticoid receptor confers resistance to antiandrogens by bypassing androgen receptor blockade. Cell 2013;155:1309–22.

46. Baca SC, Takeda DY, Seo JH, Hwang J, Ku SY, Arafeh R, et al. Reprogramming of the FOXA1 cistrome in treatment-emergent neuroendocrine prostate cancer. Nat Commun 2021;12:1979.

47. Consortium GT. The Genotype-Tissue Expression (GTEx) project. Nat Genet 2013;45:580–5.

48. Bush EC, Ray F, Alvarez MJ, Realubit R, Li H, Karan C, et al. PLATE-Seq for genome-wide regulatory network analysis of high-throughput screens. Nat Commun 2017;8:105.

49. Kruczek K, Ratterman M, Tolzien K, Sulo S, Lestingi TM, Nabhan C. A phase II study evaluating the toxicity and efficacy of single-agent temsirolimus in chemotherapy-naive castration-resistant prostate cancer. Br J Cancer 2013;109:1711–6.

50. Rathkopf DE, Picus J, Hussain A, Ellard S, Chi KN, Nydam T, et al. A phase 2 study of intravenous panobinostat in patients with castration-resistant prostate cancer. Cancer Chemother Pharmacol 2013;72:537–44.

51. Mu P, Zhang Z, Benelli M, Karthaus WR, Hoover E, Chen CC, et al. SOX2 promotes lineage plasticity and antiandrogen resistance in TP53- and RB1-deficient prostate cancer. Science 2017;355:84–8.

52. Bekes M, Langley DR, Crews CM. PROTAC targeted protein degraders: the past is prologue. Nat Rev Drug Discov 2022;21:181–200.

53. Crooke ST, Witztum JL, Bennett CF, Baker BF. RNA-targeted therapeutics. Cell Metab 2018;27:714–39.

54. Obradovic A, Ager C, Turunen M, Nirschl T, Khosravi-Maharlooei M, Jackson C, et al. Systematic elucidation and pharmacological targeting of tumor-infiltrating regulatory T cell master regulators. bioRxiv 2022;2022.02.22.481404.

55. Ding H, Burgenske DM, Zhao W, Subramaniam PS, Bakken KK, He L, et al. Single-cell based elucidation of molecularly-distinct glioblastoma states and drug sensitivity. BioRxiv 675439 [Preprint]. 2019. Available from: https://doi.org/10.1101/675439.

56. Echeverria GV, Ge Z, Seth S, Zhang X, Jeter-Jones S, Zhou X, et al. Resistance to neoadjuvant chemotherapy in triple-negative breast cancer mediated by a reversible drug-tolerant state. Sci Transl Med 2019;11.

57. Risom T, Langer EM, Chapman MP, Rantala J, Fields AJ, Boniface C, et al. Differentiation-state plasticity is a targetable resistance mechanism in basal-like breast cancer. Nat Commun 2018;9:3815.

58. Brichta L, Shin W, Jackson-Lewis V, Blesa J, Yap EL, Walker Z, et al. Identification of neurodegenerative factors using translatome-regulatory network analysis. Nat Neurosci 2015;18:1325–33.

59. Mishra V, Re DB, Le Verche V, Alvarez MJ, Vasciaveo A, Jacquier A, et al. Systematic elucidation of neuron-astrocyte interaction in models of amyotrophic lateral sclerosis using multi-modal integrated bioinformatics workflow. Nat Commun 2020;11:5579.

60. Repunte-Canonigo V, Shin W, Vendruscolo LF, Lefebvre C, van der Stap L, Kawamura T, et al. Identifying candidate drivers of alcohol dependence-induced excessive drinking by assembly and interrogation of brain-specific regulatory networks. Genome Biol 2015;16:68.

61. Son J, Ding H, Farb TB, Efanov AM, Sun J, Gore JL, et al. BACH2 inhibition reverses beta cell failure in type 2 diabetes models. J Clin Invest 2021;131:e153876.

62. Rodon J, Soria JC, Berger R, Miller WH, Rubin E, Kugel A, et al. Genomic and transcriptomic profiling expands precision cancer medicine: the WINTHER trial. Nat Med 2019;25:751–8.

63. Ma J, Fong SH, Luo Y, Bakkenist CJ, Shen JP, Mourragui S, et al. Few-shot learning creates predictive models of drug response that translate from high-throughput screens to individual patients. Nat Cancer 2021;2:233–44.

64. Warren A, Chen Y, Jones A, Shibue T, Hahn WC, Boehm JS, et al. Global computational alignment of tumor and cell line transcriptional profiles. Nat Commun 2021;12:22.

65. Chua CW, Shibata M, Lei M, Toivanen R, Barlow LJ, Bergren SK, et al. Single luminal epithelial progenitors can generate prostate organoids in culture. Nat Cell Biol 2014;16:951–61.

66. Tran C, Ouk S, Clegg NJ, Chen Y, Watson PA, Arora V, et al. Development of a second-generation antiandrogen for treatment of advanced prostate cancer. Science 2009;324:787–90.

67. Yu K, Toral-Barza L, Discafani C, Zhang WG, Skotnicki J, Frost P, et al. mTOR, a novel target in breast cancer: the effect of CCI-779, an mTOR inhibitor, in preclinical models of breast cancer. Endocr Relat Cancer 2001;8:249–58.

68. Li S, Fong KW, Gritsina G, Zhang A, Zhao JC, Kim J, et al. Activation of MAPK signaling by CXCR7 leads to enzalutamide resistance in prostate cancer. Cancer Res 2019;79:2580–92.

69. Bruzzese F, Pucci B, Milone MR, Ciardiello C, Franco R, Chianese MI, et al. Panobinostat synergizes with zoledronic acid in prostate cancer and multiple myeloma models by increasing ROS and modulating mevalonate and p38-MAPK pathways. Cell Death Dis 2013;4:e878.

70. Garcia-Gomez A, Quwaider D, Canavese M, Ocio EM, Tian Z, Blanco JF, et al. Preclinical activity of the oral proteasome inhibitor MLN9708 in myeloma bone disease. Clin Cancer Res 2014;20:1542–54.

71. Vidal SJ, Rodriguez-Bravo V, Quinn SA, Rodriguez-Barrueco R, Lujambio A, Williams E, et al. A targetable GATA2-IGF2 axis confers aggressiveness in lethal prostate cancer. Cancer Cell 2015;27:223–39.

72. Ager CR, Obradovic AZ, Arriaga JM, Chaimowitz MG, Califano A, Abate-Shen C, et al. Longitudinal immune profiling reveals unique myeloid and T-cell phenotypes associated with spontaneous immunoediting in a prostate tumor model. Cancer Immunol Res 2021;9:529–41.